

#### EDGAR AFONSO COELHO COIMBRA

BSc in Materials Engineering

# CONFORMAL DEPOSITION OF SNO<sub>2</sub> ON PHOTONIC STRUCTURED PEROVSKITE SOLAR CELLS VIA MAGNETRON SPUTTERING

MASTER IN MATERIALS ENGINEERING

NOVA University Lisbon September, 2023



## DEPARTMENT OF MATERIALS SCIENCE

## CONFORMAL DEPOSITION OF SNO<sub>2</sub> ON PHOTONIC STRUCTURED PEROVSKITE SOLAR CELLS VIA MAGNETRON SPUTTERING

#### EDGAR AFONSO COELHO COIMBRA

BSc in Materials Engineering

Adviser: Ugur Deneb Menda

Assistant Researcher, NOVA University Lisbon

Co-adviser: Hugo Manuel Brito Águas

Associate Professor, NOVA University Lisbon

#### **Examination Committee**

Chair: Manuel João de Moura Dias Mendes

Assistant Professor, NOVA University Lisbon

Members: Gizem Nogay

Innovation Project Manager, Meyer Burger AG

Ugur Deneb Menda

Assistant Researcher, NOVA University Lisbon

## Conformal Deposition of SnO<sub>2</sub> on Photonic Structured Perovskite Solar Cells via Magnetron Sputtering

Copyright © Edgar Afonso Coelho Coimbra, NOVA School of Science and Technology, NOVA University Lisbon.

The NOVA School of Science and Technology and the NOVA University Lisbon have the right, perpetual and without geographical boundaries, to file and publish this dissertation through printed copies reproduced on paper or on digital form, or by any other means known or that may be invented, and to disseminate through scientific repositories and admit its copying and distribution for non-commercial, educational or research purposes, as long as credit is given to the author and editor.

To my grandfather Vítor, who would have loved to read it.

#### ACKNOWLEDGEMENTS

I would like to express my deepest gratitude toward my adviser Dr. Deneb Menda and my co-adviser Prof. Hugo Águas, for their constant guidance and expertise which allowed me to tackle the challenges of this work, as well as Prof. Manuel Mendes, for his advice and motivation. Both as instructors and as role models, you inspired me to do more and better throughout these last 9 months.

I would like to extend my appreciation to all the staff, teachers, researchers and colleagues working in DCM, CENIMAT and CEMOP, whose efforts allow students like me to experience and contribute to the progress of scientific knowledge, with a special thanks to the Nanophotonics and Photovoltaics group, who welcomed me and my fellow MSc students with open arms. In particular, I thank Jenny Boane, who provided the photonic substrates at the heart of this dissertation as well as plentiful data and insight on her samples, Tiago Mateus, who taught me much of what I learned about working in the clean room and who was always available to help me, as well as Jonas Deuermeier, for his valuable lessons into XPS and UPS. Without the contribution of all these people, this work would have not been possible.

I leave a heartfelt 'thank you' to my sister, my mother and my father, who for the last 23 years have offered me their love and care, in spite of any hardship. To my uncles and aunts, who helped me and my family whenever and however they could, and to whom I owe a lot: António and Peggy, Natércia and Paul, Jorge and Fátima, Elvira, Pedro and Patrícia. And to my grandparents, especially to my grandmother Natália, who always cherished me and my sister.

Last but not least, I would like to thank my student's union, AEFCT, of which I had the honor of being a member for most of my academic journey. Though I have lost count of many hours, days and nights I dedicated to it, not a single one of those moments was wasted. The challenges, experiences and the friendships that came with them will always be worth it. Though it would require a dissertation all of its own to acknowledge everyone who helped me throughout those years, I owe a very special thanks to Sónia, Eduardo and Megui, for all the burdens we carried together, and to Maria and Daniela, who made those burdens feel so much lighter.

#### ABSTRACT

Light management through the incorporation of photonic structures is a promising, yet largely unrealized, path for reducing optical losses in perovskite solar cells (PSCs). The theoretical light-trapping effect of such structures can benefit the power conversion efficiency (PCE) of PSCs through gains in photocurrent density ( $J_{PH}$ ), thanks to longer optical lengths and decreased reflection losses, and in open circuit voltage ( $V_{OC}$ ) through photon recycling.

Computational studies have corroborated the efficiency gains from the inclusion of light-trapping structures in PSCs, emphasizing the importance of conformal deposition of the device layers in order to achieve maximum PCE. While colloidal lithography has been demonstrated to be a viable and scalable technique for the fabrication of the structured layers, namely on the substrate and front electrode, the issue of achieving a conformal and compact charge transport layer remains.

In this work, we demonstrate the fabrication of proof-of-concept perovskite solar cells with a conformal layer of SnO<sub>2</sub> electron transport layer deposited on top of indium tin oxide (ITO) light-trapping structures manufactured via colloidal lithography, using radio-frequency magnetron sputtering.

These experimental devices achieved a top efficiency of 7.41% ( $V_{oc}=0.85\,V$ ,  $J_{sc}=18.07\,mA/cm^2$ , FF=48.17%) for a light-trapping substrate fabricated with  $0.9\,\mu m$  polystyrene spheres, with  $100\,nm$  ITO planar layer and  $150\,nm$  structured ITO layer, that while inferior to the planar benchmark developed with commercial ITO and sputtered  $SnO_2$  (12.4% PCE, with  $V_{oc}=1.00\,V$ ,  $J_{sc}=19.8\,mA/cm^2$  and FF=62.4%), proved the viability of the approach pursued in this work. Exploiting the potential of sputtered  $SnO_2$  as a low-temperature electron transport material, we also demonstrated its use on flexible PET substrates, achieving a PCE of 9.54% ( $V_{oc}=0.89\,V$ ,  $J_{sc}=21.61\,mA/cm^2$ , FF=49.3%).

**Keywords:** Photovoltaics, Light Management, Colloidal Lithography, Perovskite Solar Cells, RF Magnetron Sputtering

#### RESUMO

A gestão de luz através da incorporação de estruturas fotónicas é um caminho promissor para reduzir as perdas óticas em células solares em perovskite (CSPs), mas maioritariamente por concretizar. O efeito teórico de aprisionamento de luz de tais estruturas pode beneficiar a eficiência das CSPs através de aumentos na densidade de fotocorrente ( $J_{PH}$ ), graças a comprimentos óticos superiores e redução das perdas por refleção, e na tensão de circuito aberto ( $V_{OC}$ ) através da reciclagem de fotões.

Estudos computacionais corroboraram os ganhos de eficiência pela inclusão de estruturas fotónicas em CSPs, destacando a importância da deposição conformal das camadas do dispositivo para atingir a máxima eficiência. Embora a litografia coloidal tenha demonstrado ser uma técnica viável e escalável para a fabricação das camadas estruturadas, nomeadamente ao nível do substrato e elétrodo frontal, o problema de produzir uma camada de transporte de cargas compacta e conformal permanece.

Neste trabalho, demonstramos uma prova de conceito para a fabricação de células solares em perovskite com uma camada de transporte de eletrões conformal de SnO<sub>2</sub> depositado sobre estruturas fotónicas de óxido de índio e estanho (ITO) produzidas através de litografia coloidal, com recurso a pulverização catódica (*sputtering*).

Estes dispositivos experimentais atingiram uma eficiência máxima de 7.41 % ( $V_{oc}$  = 0.85 V,  $J_{sc}$  = 18.07 mA/cm², FF = 48.17 %) para substratos com estruturas fotónicas fabricadas com esferas de poliestireno de 0.9 µm, com 100 nm de ITO planar e 150 nm de ITO estruturado, que embora inferiores à referência planar desenvolvida com ITO comercial e SnO<sub>2</sub> depositado com *sputtering* (12.4 % PCE, com  $V_{oc}$  = 1.00 V,  $J_{sc}$  = 19.8 mA/cm² e FF = 62.4 %), demonstraram a viabilidade da abordagem estudada neste trabalho. Explorando o potencial do SnO<sub>2</sub> depositado por *sputtering* como um material de transporte de eletrões processado a baixa temperatura, demonstrou-se também a sua utilização em substratos flexíveis de PET, atingindo uma eficiência de 9.54 % ( $V_{oc}$  = 0.89 V,  $J_{sc}$  = 21.61 mA/cm², FF = 49.3 %).

**Palavras-chave:** Fotovoltaica, Gestão de Luz, Litografia coloidal, Células solares em perovskite, Pulverização catódica

## Contents

Li	st of	Figures	5		viii
Li	st of	Tables			xi
A	crony	ms			xii
Sy	mbo	ls			xiv
Cl	hemi	cal Sym	nbols		xv
1	Mot	ivation	n and Objectives		1
2	Intr	oductio	on		3
	2.1	Perovs	skite solar cells		. 3
	2.2	Light	management in PSCs		. 5
	2.3	Sputte	ered $SnO_2$ as an ETL		. 7
3	Mat	erials a	and Methods		8
	3.1	SnO <sub>2</sub>	deposition		. 8
	3.2	SnO <sub>2</sub>	annealing		. 9
	3.3	Perovs	skite solar cell manufacturing		. 9
	3.4	Chara	acterization	•	. 9
4	Disc	cussion	1		10
	4.1	SnO <sub>2</sub>	ETL and LT structure characterization		. 10
		4.1.1	Thickness		. 10
		4.1.2	UV-Vis spectroscopy		. 12
		4.1.3	Electrical resistance measurements		. 15
		4.1.4	SEM-EDX imaging		. 16
		4.1.5	XPS-UPS measurements		. 17
		4.1.6	AFM analysis		. 21

		4.1.7	Contact angle measurements	21	
4.2 PSC manufacturing and characterization					
		4.2.1	Rigid planar PSCs with HT-SnO <sub>2</sub>	22	
		4.2.2	PSCs with RT-SnO $_2$	25	
		4.2.3	PSCs with light-trapping structures	27	
		4.2.4	PSC stability	28	
5	Con	clusion	ns and Future Prospects	29	
Bi	bliog	raphy		31	
Aj	ppend	lices			
A	Sub	strate a	and solution preparation	39	
	<b>A.1</b>	Light-	trapping structure manufacturing	39	
		A.1.1	Substrate preparation	39	
		A.1.2	Deposition of the PS colloidal monolayer	39	
		A.1.3	Shaping of the colloidal mask	40	
		A.1.4	ITO deposition	40	
		A.1.5	Colloidal mask lift-off	40	
	A.2	Substr	rate cleaning	40	
	A.3	Solution	on preparation	41	
В	Sun	nlemer	ntary information	42	

## List of Figures

1.1	Proposed architecture of the proof-of-concept PSC with LT structures	2
2.1	Generic structure of a cubic perovskite, highlighting each atom (left), and the	
	BX6 octahedral network with A atoms (right). Taken from Akkerman & Manna	2
2.2	(2020) [21]	3
2.2	Schematic illustration of the three most common PSC architectures (planar n-i-p, mesoporous n-i-p and inverted p-i-n). Adapted from Sławek et al. (2021)	
	[26]	4
2.3	Two types of photonic-patterned substrates studied by Haque et al. (2020): conventional substrate configuration (a) and inverted substrate configuration	
	(b). Taken from Haque et al. (2020) [17]	5
2.4	Energy level diagram of common materials in PSC manufacturing. Taken from	J
2.4	Wali et al. (2018) [41]	7
	(2010) [11]	,
4.1	Growth rate of the $SnO_2$ layer sputtered a) at a fixed pressure of $4 \times 10^{-3}$ mbar	
4.2	Ar and varying RF power, and b) as a function of Ar pressure and RF power. Growth rate of the SnO <sub>2</sub> layer sputtered at a fixed power of 50 W, with varying	10
	pressure and $O_2$ sputtering gas content	11
4.3	UV-Vis spectra of a SnO <sub>2</sub> sample deposited at $50 \mathrm{W}$ , $4 \times 10^{-3} \mathrm{mbar}$ Ar (with	
	T+R+A = 100 %)	12
4.4	a) Transmittance at $500  \text{nm}$ ( $T_{500}$ ) for $\text{SnO}_2$ samples sputtered a) at varying	
	power and Ar pressure (with $0\% O_2$ ), and b) at varying working pressure and	
	O <sub>2</sub> gas content at a fixed power of 50 W	13
4.5	Transmittance at $500 \text{ nm}$ ( $T_{500}$ ) for selected $SnO_2$ samples, as-deposited and	
	after annealing for 2 h at 200 °C, 350 °C and 500 °C under ambient atmosphere.	14
4.6	Tauc plot of SnO <sub>2</sub> samples sputtered at 50 W, $4 \times 10^{-3}$ mbar, as-deposited and	
	after annealing for 2 h at 200 °C, 350 °C and 500 °C under ambient atmosphere.	14
4.7	Optical bandgap of selected SnO <sub>2</sub> samples, as-deposited and after annealing	
	for 2h at 200 °C, 350 °C and 500 °C under ambient atmosphere	15
	<b>.</b>	

4.8	Resistivity of SnO <sub>2</sub> samples sputtered at a fixed power of 50 W and $4 \times 10^{-3}$ mbar,	1.
4.0	with varying thickness, after annealing at 500 °C for 2 h	16
4.9	SEM (left) and EDX (right) mapping of the edge of the SnO <sub>2</sub> film sputtered at	1 -
4.10	$50 \text{ W}, 4 \times 10^{-3} \text{ mbar Ar.}$	17
4.10	SEM image of LT substrate manufactured by colloidal lithography (0.9 μm PS	
	spheres, with 100 nm ITO planar layer and 150 nm structured ITO layer, 150 s of	
	RIE). Examples of interstitial (red) and vacancy (blue) type defects highlighted.	17
4.11	Wide XPS surveys of the sputtered SnO <sub>2</sub> samples, as-deposited (left) and	
	following O <sub>2</sub> plasma treatment (right)	18
4.12	Narrow XPS surveys of the sputtered SnO <sub>2</sub> samples in the C 1s (left) and Ta	
	4d (right) regions	19
4.13	Deconvolution of the O 1s curve of the $50 \mathrm{W}$ , $4 \times 10^{-3} \mathrm{mbar}$ sample (left) and	
	the summary of the relative amount of oxygen in the -OH chemical state in	
	each sample (right)	19
4.14	Narrow XPS surveys of the sputtered SnO <sub>2</sub> samples in the Sn 3d (left) and	
	valence band (right) regions	20
4.15	AFM scans of SnO <sub>2</sub> sputtered at 50 W, $2 \times 10^{-3}$ mbar) (top) and at 50 W, $2 \times$	
	$10^{-3}$ mbar, $2.43 \% O_2$ ) (bottom)	21
4.16	Contact angle of sputtered SnO <sub>2</sub> samples, as-deposited and after annealing for	
	2 h at 200 °C, 350 °C and 500 °C under ambient atmosphere (left). Composition	
	of frames from the sessile drop assay conducted on $SnO_2$ sample sputtered at	
	75 W and $2 \times 10^{-3}$ mbar, captured at 25 frames per second (right)	22
4.17	Electrical performance of PSCs with varying thicknesses of sputtered SnO <sub>2</sub>	
	ETL deposited at $50 \text{W}$ , $4 \times 10^{-3} \text{mbar}$ (annealed at $500 ^{\circ}\text{C}$ for $2 \text{h}$ )	23
4.18	Electrical performance of PSCs manufactured with SnO <sub>2</sub> layers sputtered at	
	50 W, with varying pressure and O <sub>2</sub> gas content (annealed at 500 °C for 2h).	
	Top 5 solar cells from each batch considered	24
4.19	Electrical performance of PSCs manufactured with SnO <sub>2</sub> layers sputtered at	
	$50\mathrm{W},3\times10^{-3}\mathrm{mbar}$ and $2.43\%$ $\mathrm{O}_2$ , without annealing, on ITO-coated glass	
	and ITO-coated PET. Top 5 solar cells from each batch considered	26
4.20	Effect of pre-measurement light exposure on the performance of a PSC on	
	PET-ITO, with SnO <sub>2</sub> layers sputtered at 50 W, $3 \times 10^{-3}$ mbar and 2.43 % O <sub>2</sub> ,	
	without annealing	26
4.21	Original (left) and colorized (right) SEM-FIB cross-section of perovskite solar	
	cell on LT substrate (0.9 µm PS spheres, with 50 nm ITO planar layer and 150 nm	
	structured ITO layer, 200 s of RIE). Blue: ITO, yellow: SnO <sub>2</sub> , orange: MAPbI <sub>3</sub> ,	
	green: spiro-OMeTAD	27
B.1	SEM-FIB cross-section of PSC with photonic IZO structures manufactured via	
٥.1	colloidal lithography (1.3 µm spheres, 350 nm sputtered IZO, 90 s RIE) and	
	spin-coated SnO <sub>2</sub> produced in the context of the APOLO project	42

B.2	UV-Vis transmittance of the LT substrates manufactured with 0.9 µm PS spheres	
	that were considered for use in the present work	43
B.3	UV-Vis transmittance of the LT substrates manufactured with 1.3 $\mu m$ PS spheres	
	that were considered for use in the present work	44

## List of Tables

4.1	Resistivity of sputtered SnO <sub>2</sub> samples obtained by four-point probe measure-	
	ment	15
4.2	XPS quantification of sputtered $SnO_2$ samples selected for use in PSCs	18
4.3	Valence band maximum and work function of the sputtered SnO <sub>2</sub> samples	
	estimated from the UPS spectrum	20
4.4	Summary of AFM surface roughness parameters	21
4.5	Characteristics of the selected structured substrates	27
4.6	Solar performance of PSCs manufactured on the selected structured substrates,	
	with SnO <sub>2</sub> layers sputtered at 50 W, $3 \times 10^{-3}$ mbar and 2.43 % O <sub>2</sub> , without	
	annealing	28
A.1	Experimental conditions used during the two reactive ion etching (RIE) pro-	
	cesses carried out in the colloidal lithography fabrication process used for this	
	work	40
B.1	Sheet resistance of the LT substrates that were considered for use in the present	
	work	45

#### ACRONYMS

**AFM** Atomic force microscopy

CL Colloidal lithography

**DI** Deionized

**EDX** Energy-dispersive X-ray spectroscopy

ETL Electron transport layerETM Electron transport material

**FF** Fill factor

**FIB** Focused ion beam

HTL Hole transport layer

**LCOE** Levelized Cost of Energy

LT Light-trapping

**PCE** Power conversion efficiency

**PSC** Perovskite solar cell

**PV** Photovoltaic

RF Radio frequencyRIE Reactive ion etchingRPM Revolutions per minute

**SEM** Scanning electron microscope

**UPS** Ultraviolet photoelectron spectroscopy

UV-Vis Ultraviolet-visible

**XPS** X-ray photoelectron spectroscopy

## Symbols

*J<sub>PH</sub>* Photocurrent density

MW h Megawatt hour

TW Terawatt

 $V_{OC}$  Open circuit voltage

### CHEMICAL SYMBOLS

AZO Aluminum-doped zinc oxide

CaTiO<sub>3</sub> Calcium titanate (perovskite)

**c-Si** Crystalline silicon

**DMF** N,N-Dimethylformamide

**DMSO** Dimethyl sulfoxide

IPA Isopropyl alcoholITO Indium tin oxide

Lithium bis(trifluoromethanesulfonyl)imide

MAI Methylammonium iodide
MAPbI<sub>3</sub> Methylammonium lead iodide

PbI<sub>2</sub> Lead iodide

**PCBM** Phenyl-C61-butyric acid methyl ester

**PDMS** Polydimethylsiloxane

PET Polyethylene terephthalate
PTFE Polytetrafluoroethylene
PTPD Poly(tetraphenylbenzidine)

SnO<sub>2</sub> Tin (IV) oxide

HT-SnO<sub>2</sub> High temperature-processed tin (IV) oxideRT-SnO<sub>2</sub> Room temperature-processed tin (IV) oxide

**spiro-OMeTAD** 2,2′,7,7′-Tetrakis[N,N-di(4-methoxyphenyl)amino]-9,9′-

spirobifluorene

TiO<sub>2</sub> Titanium dioxide

**ZnO** Zinc oxide

## MOTIVATION AND OBJECTIVES

In early 2022, the global solar energy capacity crossed the 1 TW milestone, following a record growth of 24 % with respect to 2021. In spite of an unprecedented increase in the Levelized Cost of Energy (LCOE) as a result of post-pandemic supply chain issues and global economic inflation, solar energy remains among the cheapest energy sources (\$60/MWh in 2023) and is projected to grow as much as 43 % in the current year [1, 2]

These trends, spurred by technology and policy developments in the domain of photovoltaics over the last twenty years, cement the key role of solar power in the effort toward a global energy transition.

Currently, crystalline silicon (c-Si) technologies make up over 95 % of the market share for PV modules. With commercial efficiencies of over 22 % [3], c-Si modules are a mature PV technology, estimated to retain up to 80 % of efficiency over a 40 year lifespan [4]. Despite their long-standing domination over the PV market, conventional c-Si cells are limited by the availability of silicon metal — an energy-intensive raw material, classified as critical by the European Union since 2014 [5] —, rigid geometry of the modules, and environmental impact of their production [6].

Thin-film solar cells are a PV technology which seek to address the limitations of c-Si cells, offering high power conversion efficiency (PCE) at a low cost per watt, thanks to reduced material usage, innovative semiconductors, and roll-to-roll processing techniques. Thin-film technologies are compatible with flexible and lightweight applications, clearing the way for the easy integration of PV cells in buildings, textiles and vehicles [7, 8]

Among this new generation of solar cells, perovskite solar cells (PSCs) are seen as one of the most promising thin-film PV technologies currently under development. Since the first reported use of lead halide perovskites in a dye-sensitized solar cell by Kojima et al. (2009) [9], the efficiency of PSCs has steadily risen to a record 26.1 % by July 2023, rivalling the state-of-the-art silicon cells [10].

Thanks to simple manufacturing via solution-based, low-temperature processes, perovskite solar cells are suitable for use in a variety of rigid and flexible substrates [11]. With tunable bandgaps between 1.3 and 2.3 eV [12], PSCs also show great promise for use as top cells in Si-tandem solar cells, allowing for theoretical PCEs of over 45 % [13], well in excess of the Shockley-Queissner limit of  $\sim$ 32.9 % for a single-junction cell [14]

Both in single-junction PSCs and Si/perovskite tandems, effective light management is crucial to address optical losses, which account for an estimated 11 % of energy losses in PSCs [15].

Colloidal lithography (CL) has been shown to be an attractive method for the scalable fabrication of light-trapping structures at low temperatures compatible with flexible substrates [16] Such structures are an interesting solution for light management in PSCs, with Haque et al. (2020) computationally demonstrating a 22.8 % increase in  $J_{PH}$  by the inclusion of photonic ITO structures in a superstrate n-i-p configuration PSC with SnO<sub>2</sub> as the electron transport layer (ETL), when compared with an optimized planar cell [17]

The strive to incorporate such structures in PSCs poses an additional challenge: assuring a conformal deposition of both the charge transport layer and the perovskite absorber layer over the structured substrate.

In this work, we aimed to resolve this challenge by growing a conformal layer of  $SnO_2$  on top of ITO light-trapping structures manufactured via CL, using magnetron sputtering. The ultimate goal was the manufacturing of proof-of-concept perovskite solar cells with light-trapping structures (Figure 1.1), creating a path for future optical and efficiency gains through light management. Exploiting the potential of sputtered  $SnO_2$  as a low-temperature ETL, we also aimed to demonstrate its use on flexible PET substrates.

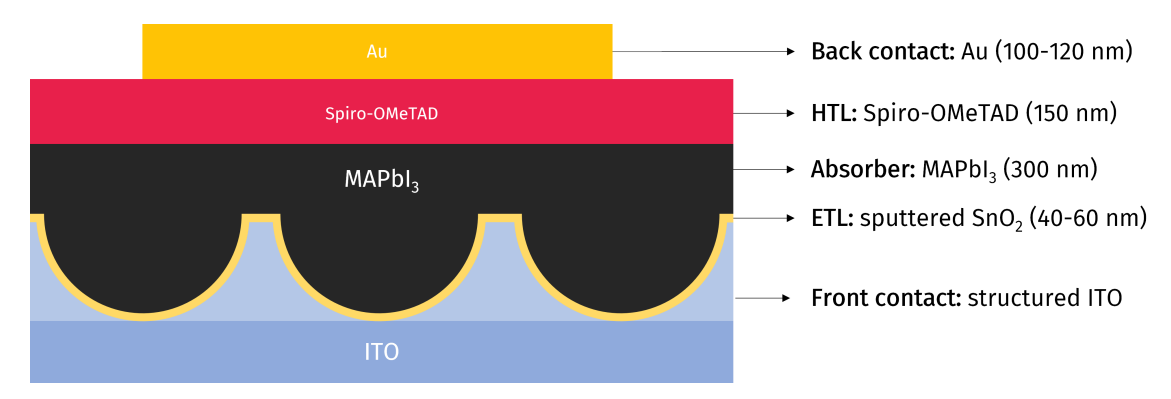


Figure 1.1: Proposed architecture of the proof-of-concept PSC with LT structures.

## Introduction

#### 2.1 Perovskite solar cells

In 2009, Kojima et al. reported the first use of lead halide perovskites in a dye-sensitized solar cell, with a power conversion efficiency of 3.81% [9]. The landmark paper of Lee at al. (2012) demonstrated the first instance of a solid-state perovskite solar cell as we recognize them today, using mesoporous  $TiO_2$  and spiro-OMeTAD as charge transport layers and achieving up to 10.9% efficiency [18]

Over the last decade, the PCE of perovskite solar cells has more than doubled, with reports of 26.1 % efficiency for a single-junction device and 33.7 % in a tandem cell [10]. The growing interest by the scientific community can be explained by the favourable optoelectronic properties of perovskites — a direct bandgap which can be tuned in a wide range (1.3 - 2.3 eV) by altering its chemical composition [12], high optical absorption coefficient, high charge mobility, long carrier diffusion lengths, good defect tolerance and low surface recombination rate — and easy deposition via wet chemical methods such as spin-coating [19, 20]

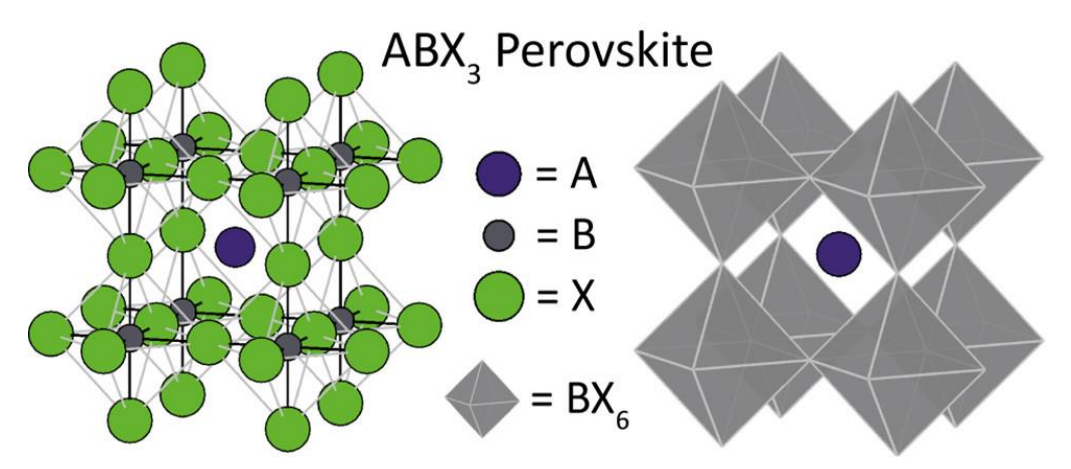


Figure 2.1: Generic structure of a cubic perovskite, highlighting each atom (left), and the BX6 octahedral network with A atoms (right). Taken from Akkerman & Manna (2020) [21]

From a material point of view, the term "perovskite" denotes a structural family of crystalline compounds similar to calcium titanate, perovskite (CaTiO<sub>3</sub>), bearing the generic formula ABX<sub>3</sub> (where A and B are cations and X is an anion). The ideal cubic perovskite structure is described as consisting of corner-sharing [BX6] octahedra (Figure 2.1), though more commonly the crystal structure shows some degree of distortion [22]

Goldschmidt's tolerance factor, t, provides an estimate of the degree of distortion (and indirectly, the tendency to form the perovskite structure). The tolerance factor is given by Equation 2.1, where  $R_A$ ,  $R_B$  and  $R_X$  are the ionic radiuses of each species. It is generally understood that 0.77 < t < 1.05 in a stable perovskite structure [23].

$$t = \frac{(R_A + R_X)}{\sqrt{2} (R_B + R_X)} \tag{2.1}$$

Perovskites are notable for being able to accommodate relatively large cations within their structure, including small organic ions, allowing for the synthesis of hybrid organic-inorganic perovskite materials. Methylammonium (MA,  $CH_3NH_3^+$ ) and formamidinium (FA,  $HC(NH_2)^{2+}$ ) are the most widely researched organic cations for lead halide perovskite solar cells [24].

Most perovskite solar cells comprise five basic components: a metal-based electrode, a hole transport layer (HTL), a light absorbing layer, an electron transport layer (ETL), and a transparent conductive oxide [25]. Figure 2.2 illustrates the three most common PSC architectures.

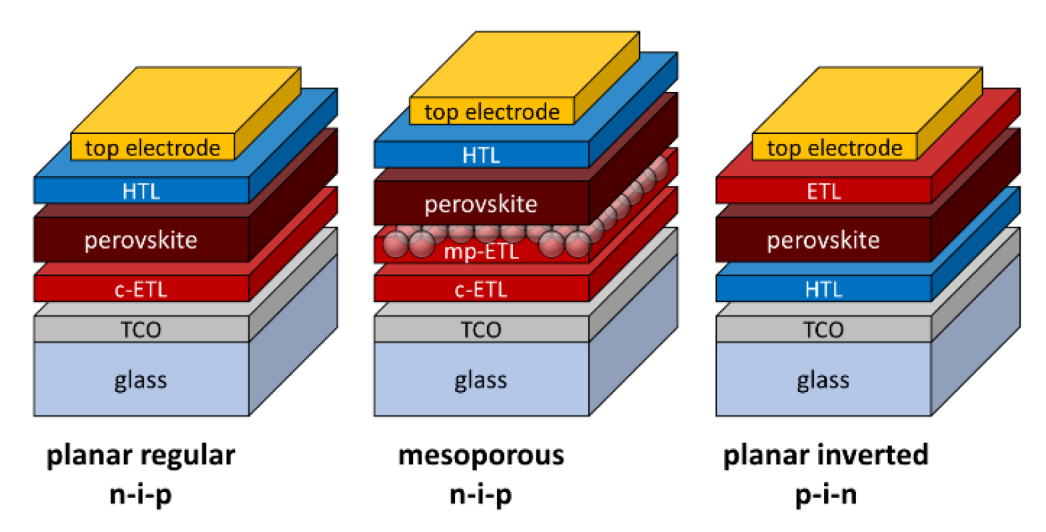


Figure 2.2: Schematic illustration of the three most common PSC architectures (planar n-i-p, mesoporous n-i-p and inverted p-i-n). Adapted from Sławek et al. (2021) [26]

Despite the favorable optoelectronic properties of lead halide perovskites, their chemical instability is a limiting factor for PSCs. The most concerning mechanisms of degradation are moisture-induced instability, thermal decomposition, and UV exposure. Oxygen exposure by itself is not considered harmful, only becoming evident when the PSC is exposed to light [27]. A wide range of encapsulation strategies have been proposed to address these issues, essentially based on insulating the cell from the environment through polymeric sealants [28].

#### 2.2 Light management in PSCs

In achieving high conversion efficiency in PSCs, a trade-off emerges between privileging photocarrier generation by effective absorption of light (favoring thicker layers of perovskite material), and ensuring high carrier collection efficiency through low recombination rates (which requires thinner perovskite films) [29]

Light-trapping strategies present a way of effectively increasing the optical thickness of the absorber layers without hindering charge collection, making them a desirable solution for improving PSC efficiency. This is especially true for tandem solar cells, where the large number of layers and the disparity between their refractive indices typically results in large optical losses from reflection and parasitic absorption [30]

Proper light management can yield gains in both  $J_{PH}$ , due to an increase in the effective optical length and decreased reflection losses, and in  $V_{OC}$ , thanks to the phenomenon of photon recycling — photons emitted by radiative recombination can be trapped and reabsorbed in the photoactive layer [31, 32]

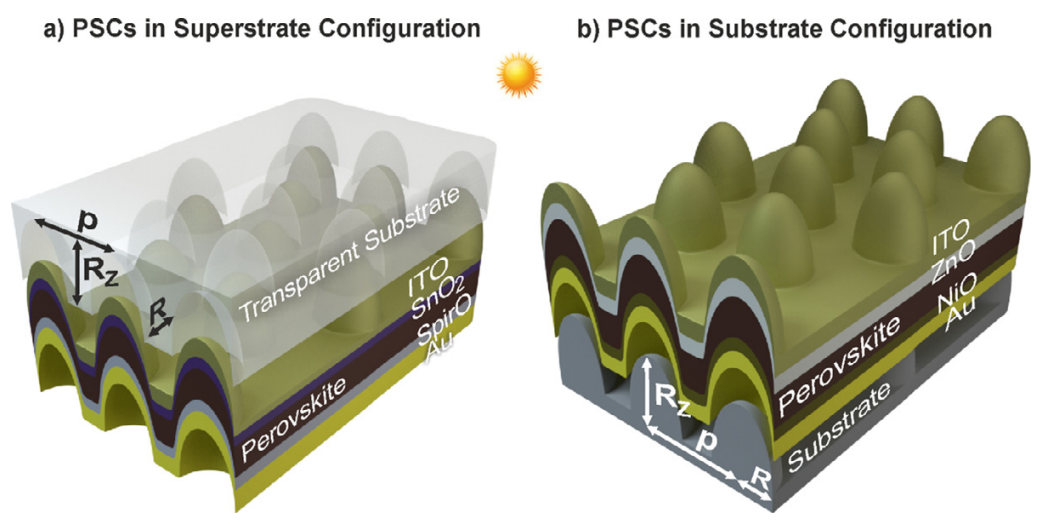


Figure 2.3: Two types of photonic-patterned substrates studied by Haque et al. (2020): conventional substrate configuration (a) and inverted substrate configuration (b). Taken from Haque et al. (2020) [17]

Considering this, a great deal of researchers' attention has been dedicated to the computational study, simulation and optimization of LT structures on PSCs.

Du et al. (2016) simulated the use of inverted vertical-cone structures, yielding 15 % to 17 % improvements in power conversion efficiency relative to planar geometries [33]. Sun et al. (2019) analyzed cylindrical nanopillar and nanohole textures manufactured with different electron transport materials, calculating a 30.48 % enhancement in efficiency of the optimized cell in comparison with planar architecture [34].

In Tooghi et al. (2020), the authors carried out a numerical study of a perovskite solar cell on nanostructured silicon substrate producible by etching, with PDMS as an anti-reflective top coating, predicting a 13.86 % to 18.29 % gain in PCE relative to a planar cell [35]. The same authors had previously simulated the effect of convex photonic-plasmonic structures with different levels of layer conformality on PSC performance, finding highly-conformable layers to yield the best results, with an increase in PCE from 14.62 % (planar) to 19.54 % (structured) [36]. Haque et al. (2020) studied the effect of photonic ITO structures in a superstrate n-i-p configuration PSC with  $SnO_2$  as the ETL (Figure 2.3), demonstrating a 22.8 % increase in  $J_{PH}$  when compared with an optimized planar cell [17].

Among these various LT structures proposed for use within PSCs, only a few have been completely or partially implemented in an experimental setting. Colloidal lithography (CL) has been shown to be an attractive method for the scalable fabrication of light-trapping structures at low temperatures compatible with flexible substrates [16]

Luo et al. (2016) used colloidal lithography to manufacture a corrugated ITO substrate, on which they deposited PTPD and MAPbI $_3$  layers. While the authors managed to achieve a corrugated interface between the HTL and the perovskite, SEM cross section images show that a consistent thickness of HTL could not be achieved by regular solution-processing [37]. Zheng et al. (2016) designed a structured ETL with TiO $_2$  nanobowls arrays via colloidal polystyrene sphere templates, showing over 3 % improvement in PCE over planar TiO $_2$  ETLs [38]. Hörantner et al. (2015) used a similar technique to produce a TiO $_2$  honeycomb structure with the goal of controlling the growth of the perovskite film to manufacture semi-transparent PSCs [39].

In the context of the APOLO project, UNINOVA has also participated in the manufacturing of PSCs with photonic IZO structures produced by CL and spin-coated with SnO<sub>2</sub>. SEM-FIB images of the finished cells proved spin-coating to be an unsuitable method for ETL deposition, yielding a layer of uneven thickness, with insufficient coverage of the photonic structure peaks (see Figure B.1 of Appendix B).

#### 2.3 Sputtered SnO<sub>2</sub> as an ETL

In PSCs, the electron transport layer fulfills the role of extracting electrons generated in the absorber layer, simultaneously blocking holes to prevent recombination. The electron transport material (ETM) must satisfy band alignment with the perovskite layer (Figure 2.4), exhibit high electron mobility [25], as well as high transmittance in the UV-Vis range to reduce optical losses in the cell [40].

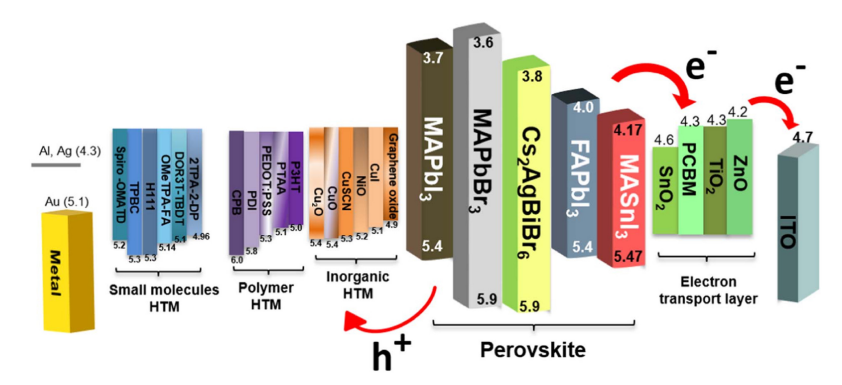


Figure 2.4: Energy level diagram of common materials in PSC manufacturing. Taken from Wali et al. (2018) [41]

The leading inorganic ETMs are the transparent metal oxides  $TiO_2$ ,  $SnO_2$  and ZnO, of which  $TiO_2$  is the most commonly reported for the manufacture of PSCs [42]. Its widespread use is explained by the high efficiencies attainable thanks to high electron injection rates and better hole blocking [41, 43]. The potential of  $TiO_2$  as an ETM is, however, limited by its low electron mobility (0.1 to  $4 \text{ cm}^2/(\text{V s})$ ) [44] and the high fabrication temperature (~500 °C) that restricts its use to rigid substrates [41]. In this context,  $SnO_2$  emerges as perhaps the most promising alternative to  $TiO_2$ .  $SnO_2$  possesses high electron mobility (25 to  $130 \text{ cm}^2/(\text{V s})$ ) [45], a wider bandgap (~3.8 eV) [41] which affords high transparency in visible wavelengths, and the ability to be effectively processed at low temperature [46].

The optoelectronic properties of intrinsic  $SnO_2$  are attributed to shallow donor states close to the conduction band, introduced by interstitial tin atoms ( $Sn_i$ ) and oxygen vacancies ( $V_O$ ), making  $SnO_2$  a conductive n-type oxide [47]. While the most common processes for manufacturing  $SnO_2$  ETLs are solution-based, sputtering deposition has proven to be a promising technique for the fabrication of functional layers in PSCs, thanks to its scalability, conformality and affordability [48].

Qiu et al. (2019) carried out a study of the performance of sputtered  $SnO_2$  as a function of working gas  $Ar/O_2$  ratio, achieving PSCs with up to 20.2 % efficiency [48], and finding an oxidizing sputtering atmosphere and low-temperature processing to be decisive factors for ETL quality. Recombination at the perovskite/sputtered  $SnO_2$  interface is one of the most significant obstacles to achieving higher efficiencies. Peng et al. (2023) demonstrated the use of PCBM as passivating layer for sputtered  $SnO_2$ , reaching 21.65 % PCE [49]

## Materials and Methods

Soda lime glass was sourced from Paul Marienfeld GmbH & Co. KG. ITO-coated glass (XY15S,  $15\,\Omega/\text{sq}$ ) and ITO-coated PET (XYP30,  $30\,\Omega/\text{sq}$ ) were sourced from Xinyan Technology LTD. Unless otherwise specified, all reagents were sourced from Sigma-Aldrich® (Merck KGaA).

The substrates and solutions for PSC manufacturing were prepared according to the procedure outlined in Appendix A.

#### 3.1 SnO<sub>2</sub> deposition

Deposition of the  $SnO_2$  electron transport layer was carried out in the homemade "3-target" RF magnetron sputtering system installed at CEMOP. The 99.99 % purity, 2" diameter  $SnO_2$  target was sourced from Super Conductor Materials, Inc.

The substrates were secured to a  $10 \times 10$  cm soda lime glass, with the target positioned at a distance of 15 cm from the center of the substrate holder. The chamber was evacuated down to a pressure of, at least,  $5 \times 10^{-6}$  mbar before initiating the sputtering process.

The working  $O_2$  and Ar gas pressures were manually regulated, and plasma ignition was carried out at 15 W by momentarily closing the gate valve. Once plasma ignition was achieved, the RF power was ramped up to the desired value at a rate of approximately 1 W/s and the target was pre-sputtered, at the desired deposition conditions, for 15 minutes in order to remove surface contamination and stabilize the conditions inside the chamber.

The sputtering process was monitored by visual inspection of the plasma and by the DC voltage bias. After the desired sputtering time, the RF power was ramped down to zero at a rate of approximately 1 W/s. The chamber was allowed to cool down for 10 minutes under vacuum before repressurization and removal of the substrates.

#### 3.2 SnO<sub>2</sub> annealing

For the manufacturing of high-temperature processed  $SnO_2$ , the samples were placed inside a Nabertherm 13/11/B170 model furnace and heated up to  $200\,^{\circ}$ C,  $350\,^{\circ}$ C or  $500\,^{\circ}$ C for the course of 1 hour, before annealing at stable temperature for an additional 2 hours. The substrates were then allowed to cool down naturally to room temperature. The entire annealing process took place under ambient atmosphere.

#### 3.3 Perovskite solar cell manufacturing

The substrates with the sputtered  $SnO_2$  layer were treated with oxygen plasma for 1.5 minutes (planar ITO-coated glass) or 3 minutes (ITO-coated PET and LT structure substrates) at 70 W and  $O_2$  pressure of 0.4 mbar, to improve their surface wettability.

The deposition of the MAPbI $_3$  layer and spiro-OMeTAD HTL was carried out via spin-coating, inside the glovebox. 135 µL of the MAPbI $_3$  solution were pipetted onto the substrate, which was spun at 1000 RPM for 10 s and then, at 5000 RPM for 20 s. At around 3 s after the spin coater had reached maximum RPM, the surface was washed with 90 µL of chlorobenzene anti-solvent. After spin-coating, the perovskite thin films were annealed at 125 °C for 10 minutes on a hotplate.

After the substrates cooled down, the spiro-OMeTAD HTL was deposited at 2000 RPM for 30 s.  $40\,\mu\text{L}$  of spiro-OMeTAD solution were pipetted onto the substrate once it had reached max RPMs, to prevent damage to MAPbI<sub>3</sub> due to reaction with the additives.

To manufacture the back contacts, masks with rectangular 0.1 cm<sup>2</sup> patterns were taped over the film surface and an 80 to 100 nm layer of Au was deposited on top via home-made e-beam evaporator. The finished perovskite solar cells were stored inside a vacuum-sealed desiccator (for short-term storage) or inside the glovebox (for long-term storage).

#### 3.4 Characterization

SnO<sub>2</sub> thickness was measured in the Ambios XP-Plus 200 Stylus profilometer. UV-Vis transmittance and reflectance measurements were carried out in the Shimadzu UV 3101PC, using the ISR-260 Integrating Sphere attachment. Resistivity was measured with the Jandel FPP 5000 four-point probe. XPS-UPS surveys were taken by the Kratos AXIS Supra instrument. Sessile drop contact angle measurements were made in the Dataphysics OCA15Plus, using ellipse fitting. Solar cell performance was measured in Newport's Oriel® VeraSol solar simulator, under 100 mW/cm<sup>2</sup> (1.0 Sun) illumination. AFM measurements were carried out in the Asylum MFP3D. SEM-EDX measurements were performed in the Hitachi TM 3030Plus Tabletop. Cross-sectional SEM-FIB images were taken in the Zeiss Auriga CrossBeam Workstation.

#### Discussion

#### 4.1 SnO<sub>2</sub> ETL and LT structure characterization

#### 4.1.1 Thickness

Current literature indicates that the performance of the electron transport layer in a PSC is strongly related to its thickness. A thin ETL may lead to insufficient surface coverage, enabling direct contact between the perovskite and the electrode (with a negative impact on hole blocking) [50], whilst an excessively thick layer will increase the series resistance and parasitic light absorption in the cell [51, 52].

Given this, the ability to closely calibrate the thickness of the sputtered  $SnO_2$  layer is an important consideration to optimize the performance of PSCs. In this section, we will discuss the effect of studied deposition parameters on the growth rate of  $SnO_2$  in the context of the current theoretical knowledge on sputtering deposition.

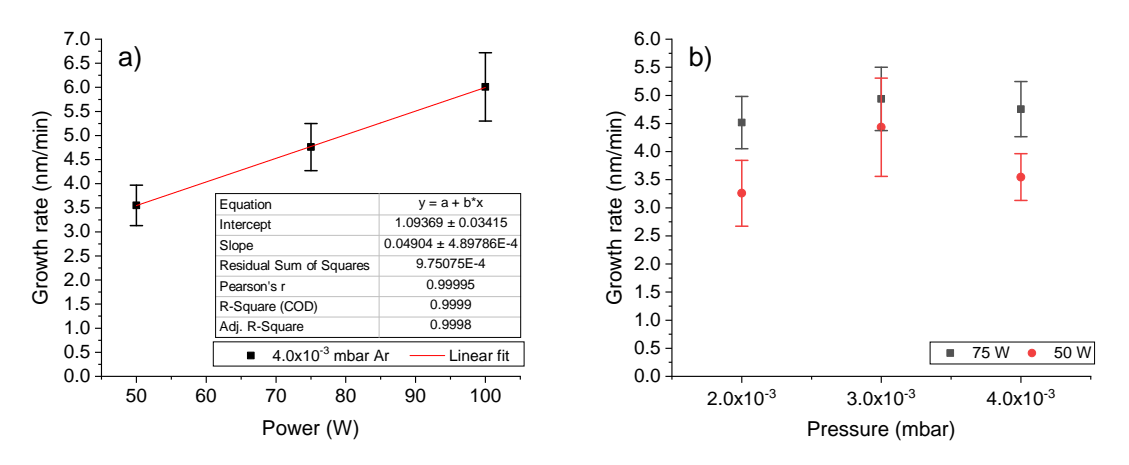


Figure 4.1: Growth rate of the  $SnO_2$  layer sputtered a) at a fixed pressure of  $4 \times 10^{-3}$  mbar Ar and varying RF power, and b) as a function of Ar pressure and RF power.

In the energy ranges typically used for sputter deposition (40 eV to 1000 eV), the sputter deposition rate is roughly proportional to the discharge power of the system [53]. When depositing  $SnO_2$  at a fixed Ar pressure of  $4 \times 10^{-3}$  mbar, the growth rate follows the expected trend, increasing linearly as a function of the RF power (Figure 4.1a) at a rate of approximately  $0.49 \,\text{Å/(min W)}$ .

The effect of the working gas pressure on sputtering yield is typically more complex. When comparing the growth rates of  $SnO_2$  layers deposited at  $50\,W$  and  $75\,W$  with varying Ar pressures, an initial increase in sputtering deposition rate can be observed between  $2\times10^{-3}$  mbar and  $3\times10^{-3}$  mbar, followed by a decrease at  $4\times10^{-3}$  mbar (Figure 4.1b).

Similar results have been reported for a variety of sputtered materials, including ITO [54], titanium-doped indium oxide [55] and AZO [56]. In theoretical terms, the initial rise in sputter yield as the pressure increases is explained by a higher density of Ar<sup>+</sup> ions capable of sputtering atoms from the target surface; as the pressure increases further, the mean free path of these ions decreases, reducing the number of collisions with the target and lowering the sputter yield [56].

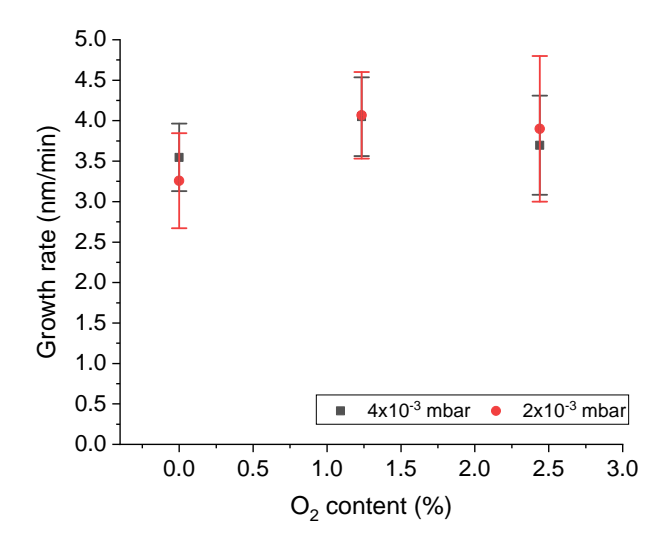


Figure 4.2: Growth rate of the SnO<sub>2</sub> layer sputtered at a fixed power of 50 W, with varying pressure and O<sub>2</sub> sputtering gas content.

In metallic targets, the effect of reactive gas content on sputtering rate has a well-established theoretical model, characterized by a sudden drop in deposition rate when a critical reactive gas flow is reached, at which point it reacts with the target to form a compound layer [53].

For the ceramic  $SnO_2$  target used in this work, we find that increasing  $O_2$  gas content has a similar (albeit less significant) effect to increasing working pressure. Hippler et al. (2019) found the energy distribution and pressure dependence of  $O^+$  ions to be similar to  $Ar^+$  ions in a  $O_2/Ar$  gas mixture [57]. In the absence of extensive reactivity between  $O_2$  and the  $SnO_2$  target, the effect on the growth rate suggests some level of sputtering contribution from oxygen ions.

#### 4.1.2 UV-Vis spectroscopy

In a n-i-p superstrate PSC, the optical properties of the ETL have a direct impact on the performance of the cell, as parasitic absorption limits the spectrum of light that reaches the perovskite layer. In a wider sense, UV-Vis measurements can provide important insights into the optoelectronic properties of the ETL, namely its optical bandgap.

In this section, we will compare the UV-Vis spectra of sputtered  $SnO_2$  samples deposited at varying power, Ar pressure and  $O_2$  concentration, estimate the optical bandgap via Tauc plot, and discuss the effect of annealing on the aforementioned properties. All  $SnO_2$  samples were deposited on soda lime glass, with an approximate thickness of 40 nm.

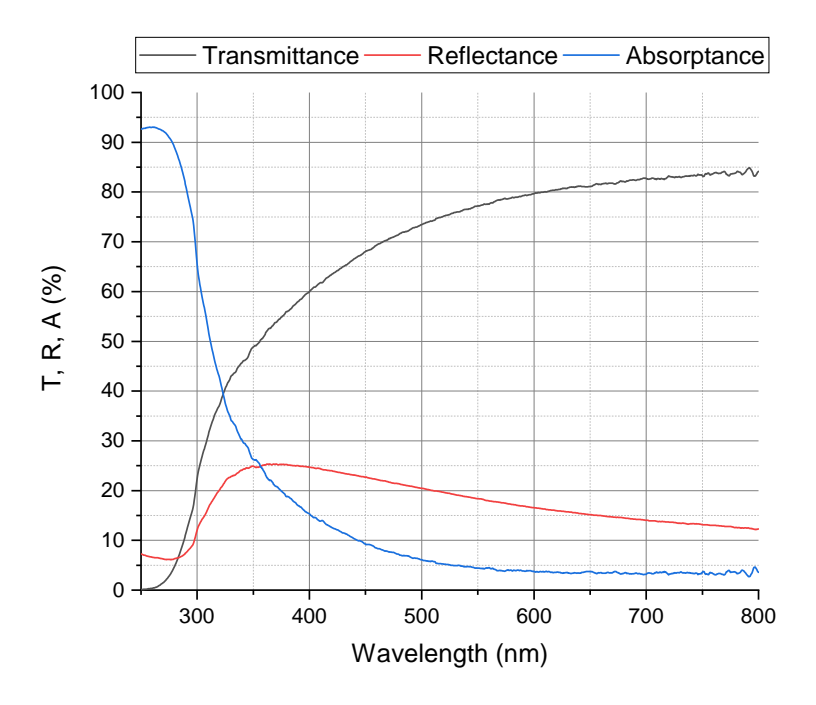


Figure 4.3: UV-Vis spectra of a  $SnO_2$  sample deposited at 50 W,  $4 \times 10^{-3}$  mbar Ar (with T+R+A = 100%).

Figure 4.3 illustrates the typical UV-Vis spectra measured from the sputtered  $SnO_2$  samples, showing high transmittance (> 70%) over most of the visible range of wavelengths and high absorption in the ultraviolet range. A common figure of comparison for transparent oxides is the transmittance at the solar maximum ( $\sim 500 \, \text{nm}$ ).

We find  $T_{500}$  to be dependent on both RF power and Ar pressure, with highest transmittance measured at 50 W and  $3 \times 10^{-3}$  mbar (Figure 4.4). Likewise, working pressure and oxygen gas content exhibit a strong effect on  $T_{500}$ , showing maximum transmittance at  $4 \times 10^{-3}$  mbar and  $2.43 \% O_2$  (50 W).

In  $SnO_2$ , the density of oxygen vacancies has a strong effect on the absorption of light by the film; as such, the results in Figure 4.4 suggest that even a low  $O_2$  gas content (< 3%) can effectively suppress oxygen vacancies, especially at higher working pressures.

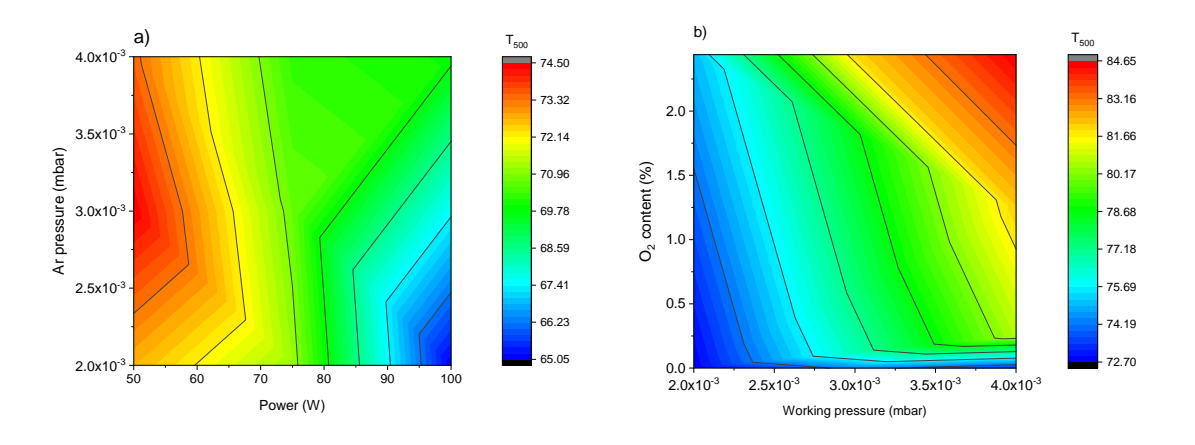


Figure 4.4: a) Transmittance at  $500 \, \text{nm}$  ( $T_{500}$ ) for  $SnO_2$  samples sputtered a) at varying power and Ar pressure (with  $0 \, \% \, O_2$ ), and b) at varying working pressure and  $O_2$  gas content at a fixed power of  $50 \, \text{W}$ .

The effect of thermal treatment on the transmittance of selected  $SnO_2$  samples was also studied by annealing them for 2 h at 200 °C, 350 °C and 500 °C under ambient conditions. In Figure 4.5, for samples sputtered under pure Ar gas (S2-S6), we find considerable gains in  $T_{500}$  as the annealing temperature increases, up to 10 % in samples annealed at 500 °C when compared with the pristine samples. The effect of annealing on  $SnO_2$  samples sputtered in a  $O_2$ /Ar mixture (S7-S9) is comparatively small (< 3 % increase in  $T_{500}$ ).

Priyadarshini et al. (2017) has demonstrated that oxygen vacancies in  $SnO_2$  films are suppressed by annealing in the presence of  $O_2$  gas [58]. The reduced responsiveness of  $O_2$ /Ar-sputtered samples to annealing treatment could thus be attributed to the lower density of oxygen vacancies available to react with atmospheric  $O_2$ .

The optical bandgap of the sputtered  $SnO_2$  samples can be estimated from their respective Tauc plots. Since  $SnO_2$  is considered a direct bandgap semiconductor, we use  $(\alpha hv)^2$  as the dependent variable (Figure 4.6).

By extrapolating the linear region of the Tauc plot for each sample, we can estimate the bandgap as the point where the line crosses the x-axis. Figure 4.7 summarizes the estimated optical bandgap of selected SnO<sub>2</sub> samples, before and after annealing.

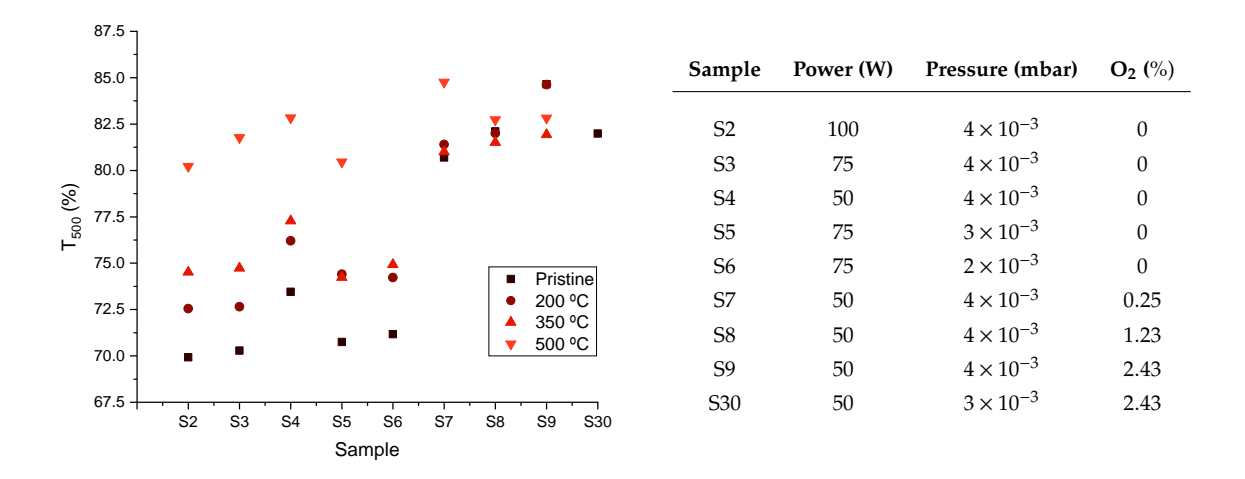


Figure 4.5: Transmittance at 500 nm ( $T_{500}$ ) for selected SnO<sub>2</sub> samples, as-deposited and after annealing for 2 h at 200 °C, 350 °C and 500 °C under ambient atmosphere.

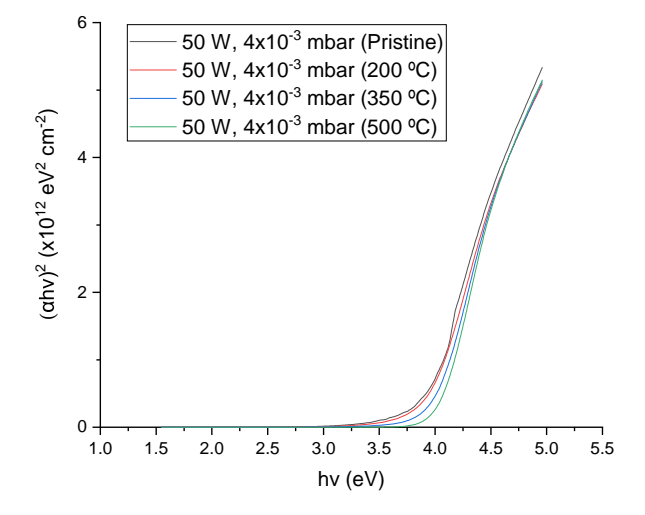


Figure 4.6: Tauc plot of  $SnO_2$  samples sputtered at  $50 \, \text{W}$ ,  $4 \times 10^{-3} \, \text{mbar}$ , as-deposited and after annealing for 2 h at  $200 \, ^{\circ}\text{C}$ ,  $350 \, ^{\circ}\text{C}$  and  $500 \, ^{\circ}\text{C}$  under ambient atmosphere.

The calculated bandgaps range from 3.8 eV to 4.06 eV, a value consistent with measurements reported in the literature. Interestingly, for pure Ar-sputtered samples (S2-S6), annealing results in a significant increase of the optical bandgap, which is accompanied by a sharp rise in conductivity (see 4.1.3 - Electrical resistance measurements). The rise in apparent bandgap could therefore be attributable to an increase in charge carrier concentration, populating the lowest states of the conduction band (Burstein-Moss shift), as reported by Park et al. (2014) for ITO and Lyubchyk et al. (2016) for ZnO [59, 60]

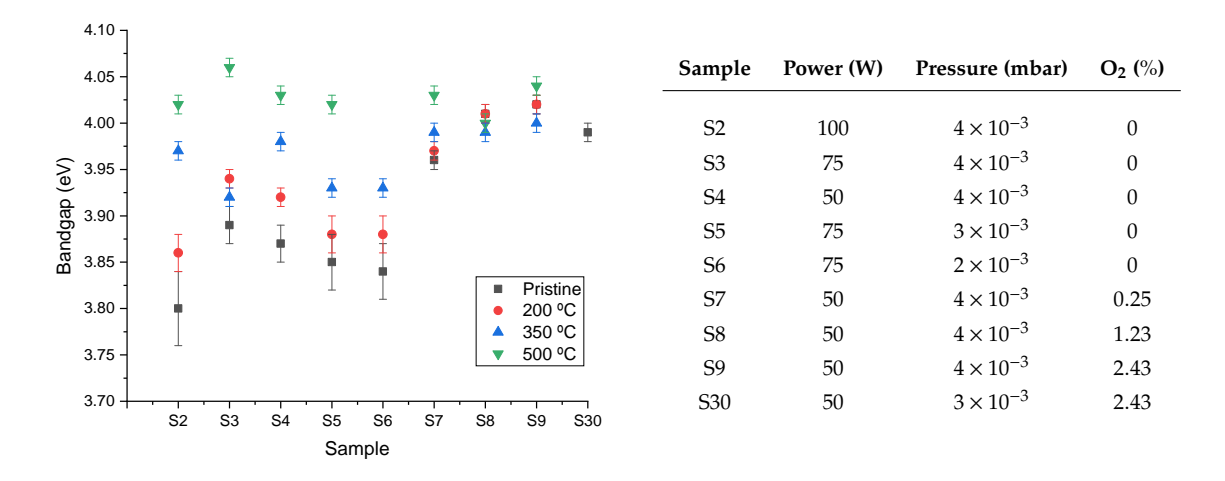


Figure 4.7: Optical bandgap of selected  $SnO_2$  samples, as-deposited and after annealing for 2 h at 200 °C, 350 °C and 500 °C under ambient atmosphere.

#### 4.1.3 Electrical resistance measurements

While the electrical conductivity of the ETL is generically not considered a direct metric of its performance in a PSC, high resistivity may have a negative effect on the efficiency of the cell by contributing to its series resistance, making it a relevant factor.

As such, in this section we will briefly analyze the resistivity of various sputtered  $SnO_2$  layers manufactured throughout the work. Table 4.1 summarizes the resistivity measurements obtained by four-point probe.

Table 4.1: Resistivity of sputtered SnO<sub>2</sub> samples obtained by four-point probe measurement.

Sample	Power (W)	Pressure (mbar)	$O_2$ %	Treatment	<b>Resistivity</b> ( $\Omega$ cm)
S2	100	$4 \times 10^{-3}$	0	< 500 °C	Insulating
				500 °C	0.01
S3	75	$4 \times 10^{-3}$	0	< 500 °C	Insulating
				500 °C	Insulating
S4	50	$4 \times 10^{-3}$	0	< 500 °C	Insulating
				500°C	0.10
S5	75	$3 \times 10^{-3}$	0	< 500 °C	Insulating
				500°C	0.08
S6	75	$2 \times 10^{-3}$	0	< 350 °C	Insulating
				350°C	0.43
				500°C	0.02
S7	50	$4 \times 10^{-3}$	0.25	< 500 °C	Insulating
				500°C	1.93
S8	50	$4 \times 10^{-3}$	1.23	< 500 °C	Insulating
				500°C	0.52
S9	50	$4 \times 10^{-3}$	2.43	< 500 °C	Insulating
				500°C	0.99
S25	50	$2 \times 10^{-3}$	0	< 500 °C	Insulating
				500°C	0.01
S26	50	$2 \times 10^{-3}$	2.43	< 500 °C	Insulating
				500°C	135.40
S30	50	$3 \times 10^{-3}$	2.43	Pristine	0.18

It is important to note that almost every sample\* was too insulating to be effectively measured by four-point probe, with their electrical conductivity increasing by several orders of magnitude when annealed for 2 h at  $500\,^{\circ}$ C. For pure Ar-sputtered samples, the resistivity of these high temperature-processed (HT-SnO<sub>2</sub>) layers is within the typical range that has been reported in the literature for several years ( $10^{-2}$  to  $10^{-4}\,\Omega$  cm) [61]

Equally important is the finding of, at least, one set of sputtering conditions which reliably produces conductive as-deposited films — S30 (50 W,  $3 \times 10^{-3}$  mbar, 2.43 % O<sub>2</sub>). This room temperature-processed (RT-SnO<sub>2</sub>) layer, in turn, also displays high transmittance (T<sub>500</sub> > 80 %, see 4.1.2 to UV-Vis spectroscopy), making it highly promising for use in PSCs.

Figure 4.8 depicts the relation between the thickness of the deposited  $SnO_2$  film and the resistivity measured. Between 25 nm and 30 nm, we observe a sudden drop in the resistivity of the layers, which roughly stabilizes at greater thicknesses. Such behavior has been observed in other sputtered materials, namely Al [62], Au [63] and ITO [64], being attributable to the coalescence of the islands of sputtered material deposited on the substrate into an electrically continuous film.

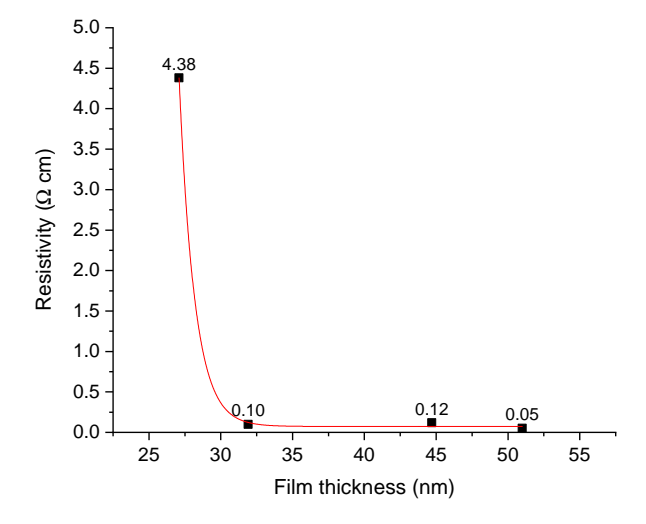


Figure 4.8: Resistivity of  $SnO_2$  samples sputtered at a fixed power of 50 W and  $4 \times 10^{-3}$  mbar, with varying thickness, after annealing at 500 °C for 2 h.

#### 4.1.4 SEM-EDX imaging

At the beginning of the work, tabletop SEM-EDX measurements were taken of the planar sputtered  $SnO_2$  layers and of the ITO LT structures to assess their rough morphologies, with the images of the sputtered  $SnO_2$  layers on glass showing a compact film deposited over the surface (Figure 4.9).

<sup>\*</sup>Pristine or annealed below 500 °C

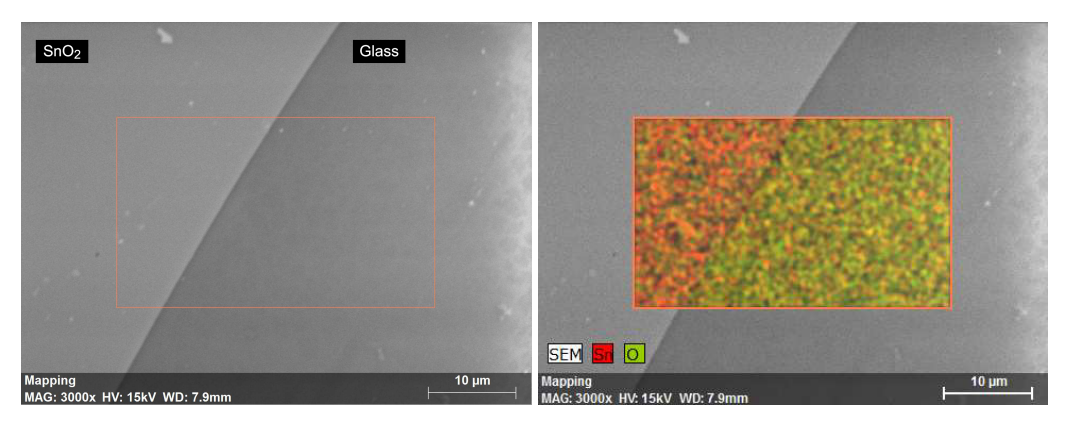


Figure 4.9: SEM (left) and EDX (right) mapping of the edge of the SnO<sub>2</sub> film sputtered at 50 W,  $4 \times 10^{-3} \text{ mbar Ar}$ .

In the case of LT structure substrates, the surface presents arrays of honeycomb-patterned ITO with different orientations (Figure 4.10), comparable to grains in a crystal lattice. These arrays also exhibit similar defects to atomic crystals, with interstitial and vacancy-type defects present. Such imperfections typically occur in colloidal lithography as a result of array mismatch as the templating spheres self-assemble over different areas of the surface and destabilization of the spheres by Brownian forces [16, 65]

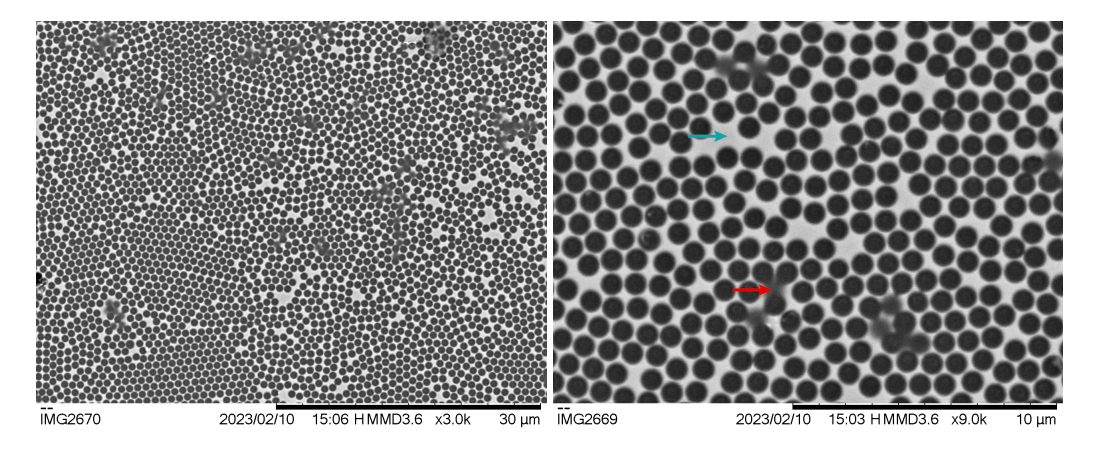


Figure 4.10: SEM image of LT substrate manufactured by colloidal lithography ( $0.9 \, \mu m$  PS spheres, with  $100 \, nm$  ITO planar layer and  $150 \, nm$  structured ITO layer,  $150 \, s$  of RIE). Examples of interstitial (red) and vacancy (blue) type defects highlighted.

#### 4.1.5 XPS-UPS measurements

To study the surface chemistry of the sputtered  $SnO_2$  films, XPS surveys of the layers selected for use in PSCs (see 4.2 - PSC manufacturing and characterization) were undertaken, before and after  $O_2$  plasma treatment. Due to technical issues with the equipment utilized, UPS measurements were only performed on the plasma-treated samples. The spectrum of the wide XPS surveys can be seen in Figure 4.11, with the resulting quantification in Table 4.2. Based on their binding energy, the photoelectron peaks present in the survey can be attributed to four elements: O, C, Sn and Ta.

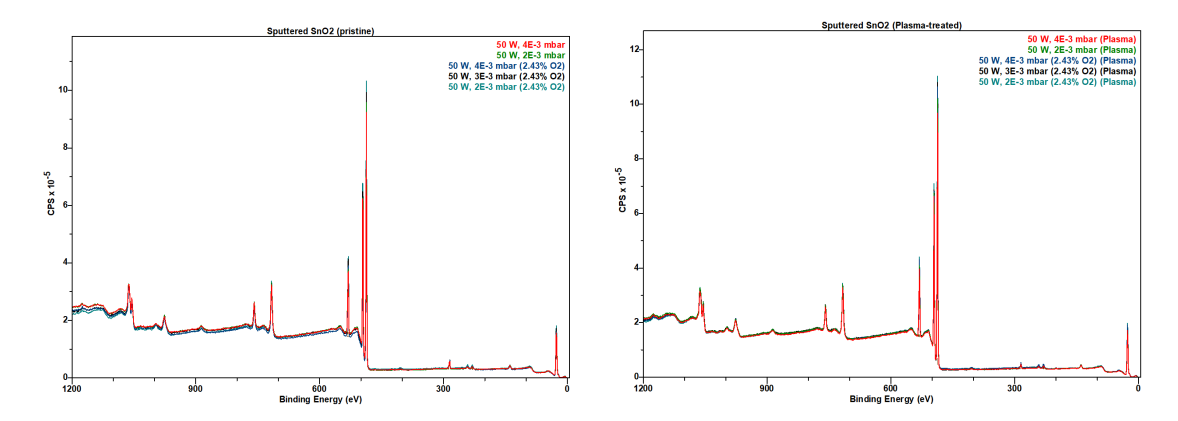


Figure 4.11: Wide XPS surveys of the sputtered  $SnO_2$  samples, as-deposited (left) and following  $O_2$  plasma treatment (right).

Table 4.2: XPS quantification of sputtered SnO<sub>2</sub> samples selected for use in PSCs

Sample	Region	%At Conc (Pristine)	%At Conc (Plasma)	Sn:O <sub>x</sub> (Pristine)	Sn:O <sub>x</sub> (Plasma)
$50 \text{ W}, 4 \times 10^{-3} \text{ mbar}$	C 1s	20.56	11.90	1.79	1.98
	O 1s	50.42	57.98		
	Sn 3d	28.23	29.22	-	
	Ta 4d	0.78	0.9	•	
$50 \text{ W}, 2 \times 10^{-3} \text{ mbar}$	C 1s	19.84	10.48	1.76	1.94
	O 1s	50.79	58.44	-	
	Sn 3d	28.78	30.2	•	
	Ta 4d	0.59	0.89	•	
$50 \text{ W}, 4 \times 10^{-3} \text{ mbar } (2.43\% \text{ O}_2)$	C 1s	21.55	12.9	2.05	1.99
	O 1s	51.93	57.1	•	
	Sn 3d	25.37	28.65	•	
	Ta 4d	1.15	1.34	-	
50 W, $3 \times 10^{-3}$ mbar (2.43% O <sub>2</sub> )	C 1s	20.91	11.49	1.99	1.96
	O 1s	52.15	58.07	•	
	Sn 3d	26.17	29.67	-	
	Ta 4d	0.76	0.66	•	
$50 \text{ W}, 2 \times 10^{-3} \text{ mbar } (2.43\% \text{ O}_2)$	C 1s	18.67	11.64	1.93	1.93
	O 1s	52.77	57.36	-	
	Sn 3d	27.4	29.71	-	
	Ta 4d	1.16	1.29	•	

The presence of adventitious carbon is expected in any sample that has been exposed to the environment, the peak of its 1s orbital being typically used to calibrate the binding energy of the remaining narrow surveys. In this case, the peak of the C 1s was calibrated to  $284.8\,\mathrm{eV}$  (C-C bond) [66] (Figure 4.12). Following treatment, the atomic concentration of C is reduced by roughly one half, as the  $O_2$  plasma removes a large quantity of organic compounds accumulated on the surface.

Evidence for trace amounts of tantalum in the SnO<sub>2</sub> layers is an unexpected, yet plausible finding (Figure 4.12). While, to the best of our knowledge, no Ta-containing compounds or equipment had been used in the same work environment as the samples, endogenous contamination from the SnO<sub>2</sub> sputtering target also cannot be ruled out. It is known that Ta and Sn-containing ores are frequently mined together, creating a plausible pathway for contamination during manufacturing [67]. The SnO<sub>2</sub> layers produced in the course of this work should, thus, be regarded as having a certain level of doping by Ta atoms, averaging less than 1 % atomic concentration (Table 4.2).

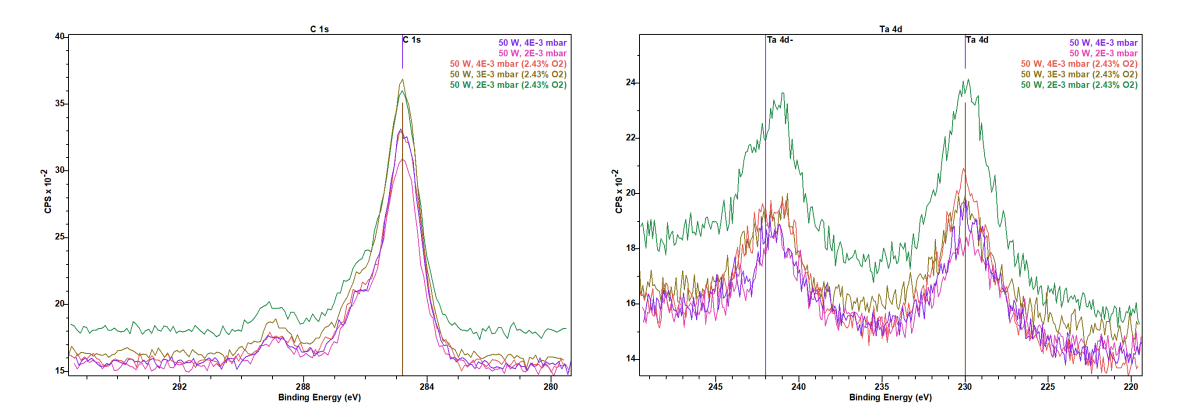


Figure 4.12: Narrow XPS surveys of the sputtered SnO<sub>2</sub> samples in the C 1s (left) and Ta 4d (right) regions.

In the O 1s survey, the oxygen signal can be fitted into two fundamental chemical states: the lattice Sn-O peak at around 530.3 eV and the chemisorbed ( $O_{chem}$ ) peak at around 531.5 eV [68]. For most samples, following  $O_2$  plasma treatment we see a slightly increase in the proportion of oxygen chemically bound on the surface, which may likely arise from the functionalization of the surface by the plasma treatment.

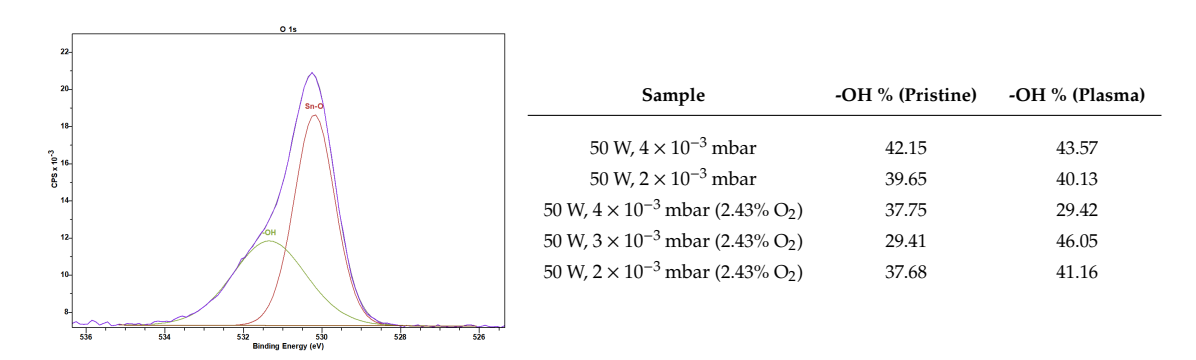


Figure 4.13: Deconvolution of the O 1s curve of the  $50 \, \text{W}$ ,  $4 \times 10^{-3} \, \text{mbar}$  sample (left) and the summary of the relative amount of oxygen in the -OH chemical state in each sample (right).

The Sn 3d narrow surveys show a well-defined feature at approximately  $486.6 \, \text{eV}$ , corresponding to the nominal binding energy of the  $\text{SnO}_2$  chemical state [68]. As the binding energy of  $\text{SnO}_2$  is relatively close to the binding energy of  $\text{SnO}(485.9 \, \text{eV})$ , the narrow survey is not the most adequate to determine the oxidation state of the Sn atoms.

A survey of the valence band reveals the existence of an extra band edge with its peak at 2 to 2.5 eV, which corresponds to the SnO state [69]; this state is apparent in the SnO<sub>2</sub> samples sputtered in the absence of O<sub>2</sub> and mostly or completely suppressed in samples sputtered with 2.43 % oxygen (Figure 4.14). This observation leads us to conclude that the addition of O<sub>2</sub> during sputtering effectively compensates for oxygen deficiency in the film, a conclusion that is further validated by the ratio of the Sn:O atoms in the wide XPS survey (Table 4.2). All samples sputtered under an Ar/O<sub>2</sub> mixture yielded films with a stoichiometry close to 1:2, in comparison to pure-Ar sputtered films, which had Sn:O ratios of 1:1.79 (50 W and  $4 \times 10^{-3}$  mbar) and 1:1.76 (50 W and  $2 \times 10^{-3}$  mbar). It is also interesting to note that, following treatment with O<sub>2</sub> plasma, all films displayed Sn:O ratios close to 1:2, showing that plasma is capable of oxidizing the surface of the SnO<sub>2</sub> layers.

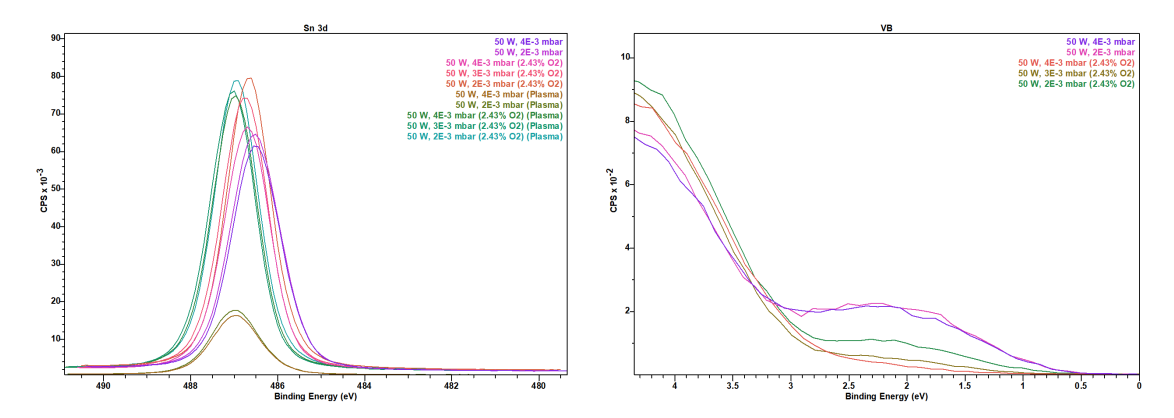


Figure 4.14: Narrow XPS surveys of the sputtered SnO<sub>2</sub> samples in the Sn 3d (left) and valence band (right) regions.

From the UPS spectra of the plasma-treated samples, it was possible to estimate the work function ( $\Phi$ ) and valence band maximum (VBM) of the SnO<sub>2</sub> layers, which are summarized in the Table 4.3.

Table 4.3: Valence band maximum and work function of the sputtered SnO<sub>2</sub> samples estimated from the UPS spectrum.

Sample	VBM (eV)	Φ (eV)
$50 \text{ W}, 4 \times 10^{-3} \text{ mbar}$	3.61	4.23
$50 \text{ W}, 2 \times 10^{-3} \text{ mbar}$	3.63	4.23
50 W, $4 \times 10^{-3}$ mbar (2.43% O <sub>2</sub> )	3.39	4.33
50 W, $3 \times 10^{-3}$ mbar (2.43% O <sub>2</sub> )	3.46	4.29
50 W, $2 \times 10^{-3}$ mbar (2.43% O <sub>2</sub> )	3.42	4.33

### 4.1.6 AFM analysis

The roughness of the electron transport layer can affect the performance of PSCs in two ways: a) high surface roughness can contribute to uneven coverage, potentially allowing contact between the perovskite and the electrode, and b) rougher surfaces can hinder the crystallization of the perovskite film. Considering this, AFM scans were performed on some of the sputtered  $SnO_2$  samples on glass, to obtain a general assessment of their surface (Figure 4.15).

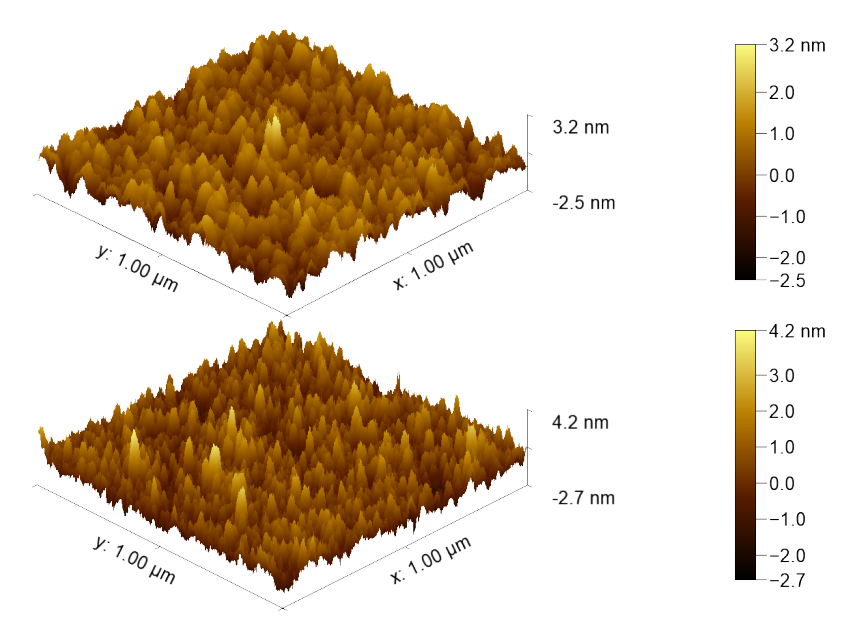


Figure 4.15: AFM scans of SnO<sub>2</sub> sputtered at 50 W,  $2 \times 10^{-3}$  mbar) (top) and at 50 W,  $2 \times 10^{-3}$  mbar, 2.43 % O<sub>2</sub>) (bottom)

Table 4.4 provides a summary of the roughness parameters that describe each of the scanned surfaces. The RMS roughness is in the typical range reported for SnO<sub>2</sub> [70], corresponding to a smooth surface.

Table 4.4: Summary of AFM surface roughness parameters.

Sample	RMS Roughness (nm)	Mean Roughness (nm)	Minimum (nm)	Maximum (nm)
$50 \mathrm{W}, 2 \times 10^{-3} \mathrm{mbar}$	0.569	0.454	-2.544	3.159
$50 \mathrm{W}, 2 \times 10^{-3} \mathrm{mbar}, 2.43 \% \mathrm{O}_2$	0.729	0.574	-2.681	4.239

### 4.1.7 Contact angle measurements

The wettability of the electron transport layer has been known to play an important role in the performance of the PSC, as highly-wettable surfaces can assist in the formation of a pinhole-free, high-quality perovskite layer [71]. To study the effect of annealing on the SnO<sub>2</sub> surface, the contact angle was measured immediately after cooldown, via sessile drop assay.

In Figure 4.16a, the sharp drop in contact angle following high temperature ( $500\,^{\circ}$ C) annealing becomes apparent, with the SnO<sub>2</sub> surface becoming highly hydrophilic. Indeed, the hydrophilicity of freshly-annealed samples could be so extreme as to preclude accurate measurement of the contact angle, often achieving contact angles of under  $5^{\circ}$  in around 300 ms (Figure 4.16b).

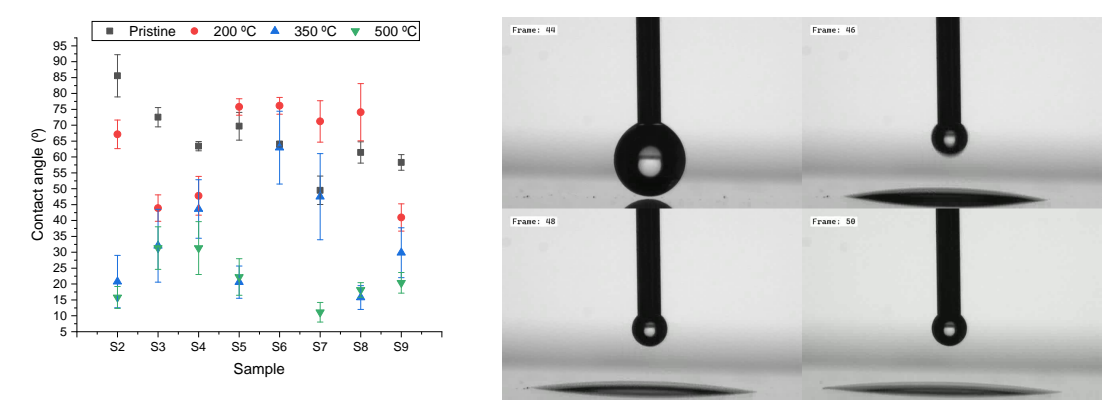


Figure 4.16: Contact angle of sputtered  $SnO_2$  samples, as-deposited and after annealing for 2 h at 200 °C, 350 °C and 500 °C under ambient atmosphere (left). Composition of frames from the sessile drop assay conducted on  $SnO_2$  sample sputtered at 75 W and  $2\times10^{-3}$  mbar, captured at 25 frames per second (right).

In sputtered  $TiO_2$  films, the wetting behavior of the surface is believed to be influenced by a concentration gradient of mobile oxygen vacancies ( $V_O$ ) across the film. When moving to the surface,  $V_O$  catalyze the hydroxylation of partially-uncoordinated metal ions by  $H_2O$  molecules; the hydroxyl groups, in turn, enhance the hydrophilic properties of the surface through increased Van der Walls and hydrogen-bonding interactions [72]. A similar mechanism may be responsible for the observed wetting properties of the  $SnO_2$  samples, with high-temperature annealing leading to increased  $V_O$  mobility and so, more extensive hydroxylation and wetting of the surface.

# 4.2 PSC manufacturing and characterization

### 4.2.1 Rigid planar PSCs with HT-SnO<sub>2</sub>

The first prototype planar cells were manufactured on ITO-coated glass substrates using  $SnO_2$  layers sputtered at 50 W and  $4\times10^{-3}$  mbar Ar, annealed at 500 °C for 2 h. These sputtering conditions were selected based on the high transmittance and conductivity post-annealing (see 4.1.2, 4.1.3).

In order to assess the effect of ETL thickness and concentration of the MAPbI<sub>3</sub> solution on the performance of the PSCs, several batches of solar cells were prepared with SnO<sub>2</sub> thicknesses between 30 and 60 nm and MAPbI<sub>3</sub> concentrations of 1 M and 1.2 M. Figure 4.17 reflects the key solar cell performance figures as function of these parameters.

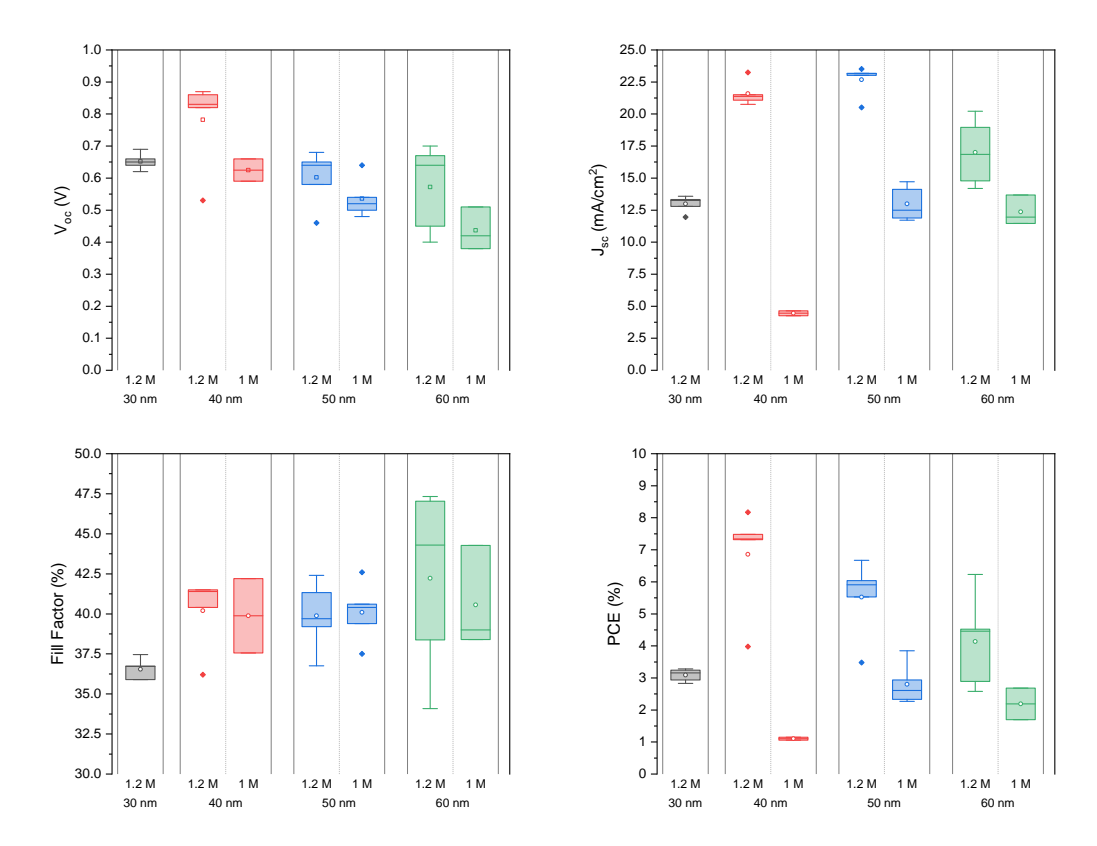


Figure 4.17: Electrical performance of PSCs with varying thicknesses of sputtered  $SnO_2$  ETL deposited at 50 W,  $4 \times 10^{-3}$  mbar (annealed at 500 °C for 2 h).

The effect of MAPbI<sub>3</sub> concentration is evident across every figure, with PSCs manufactured using 1.2 M solution of MAPbI<sub>3</sub> yielding higher  $V_{oc}$ ,  $J_{sc}$ , PCE, and better or comparable fill factor (FF). This effect is especially significant for lower thicknesses of SnO<sub>2</sub>; as a matter of fact, the cells manufactured with 30 nm-thick SnO<sub>2</sub> and 1 M MAPbI<sub>3</sub> solution were non-functional and no IV curve could be measured to extract the relevant performance figures.

The thickness of the electron transport layer is shown to also have a significant effect on the performance of the PSCs. The highest efficiency cells in this experiment were manufactured using a 40 nm layer of  $SnO_2$ , with a maximum PCE of 8.17 % ( $V_{oc} = 0.87 \, \text{V}$ ,  $J_{sc} = 23.24 \, \text{mA/cm}^2$ ,  $FF = 40.4 \, \%$ ). It is interesting to note that voltage loss is the primary cause of efficiency drop at higher thicknesses, in spite of greater fill factors being observed for 50 nm and 60 nm — we may conjecture that while these larger thicknesses of  $SnO_2$  possess more effective hole-blocking capacity, in terms of power conversion efficiency, this factor is outweighed by bulk recombination in the  $SnO_2$  film.

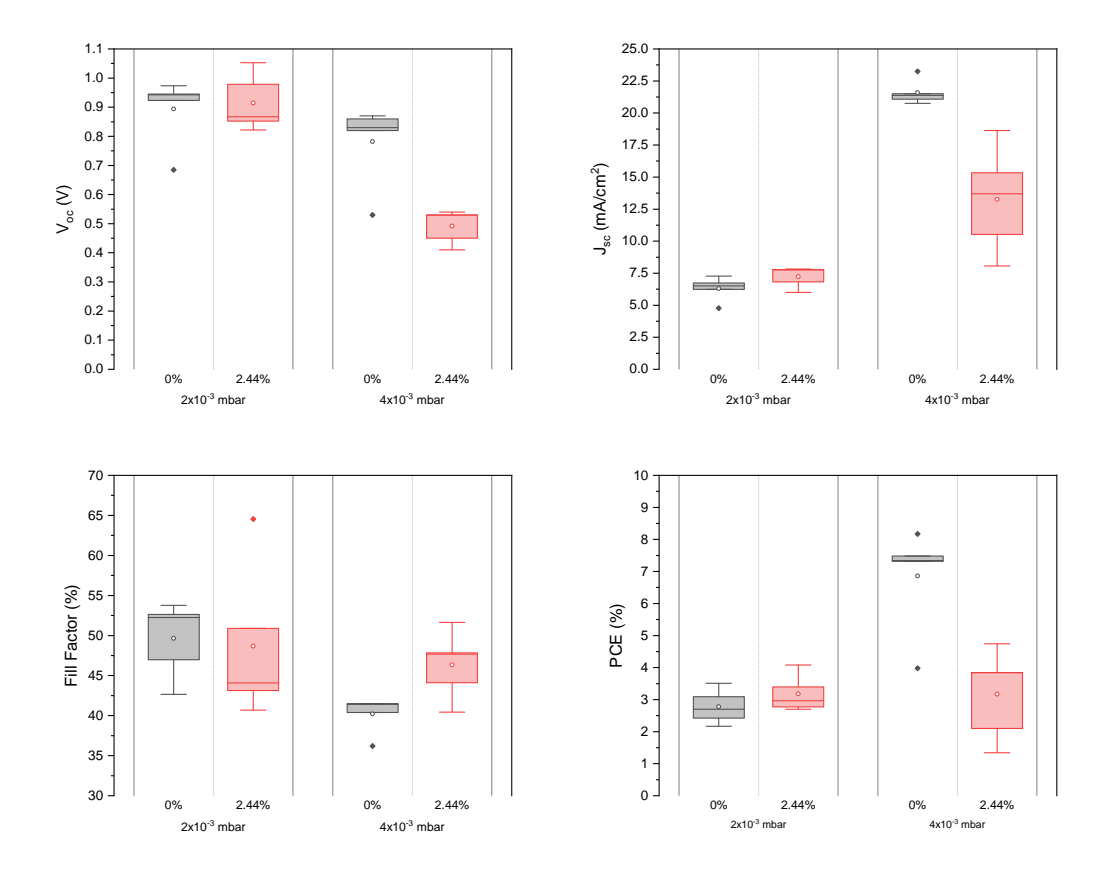


Figure 4.18: Electrical performance of PSCs manufactured with  $SnO_2$  layers sputtered at 50 W, with varying pressure and  $O_2$  gas content (annealed at  $500\,^{\circ}$ C for 2 h). Top 5 solar cells from each batch considered.

The poor performance of PSCs with  $30\,\mathrm{nm}~\mathrm{SnO_2}$  is also worthy of note. As evidenced in 4.1.3 - Electrical resistance measurements, effective coverage by the sputtered  $\mathrm{SnO_2}$  is achieved at a thickness greater than  $30\,\mathrm{nm}$ , such that the inadequate performance of these cells can be likely explained by short circuiting between the ITO contact and the perovskite layer.

Following this study, all subsequent batches of perovskite solar cells were manufactured using  $SnO_2$  thicknesses of  $40\,\mathrm{nm}$  and  $MAPbI_3$  concentrations of 1.2 M. The work proceeded by exploring some of the other promising HT-SnO<sub>2</sub> layers found during characterization, namely those deposited at  $50\,\mathrm{W}$  with a pressure  $2\times10^{-3}\,\mathrm{mbar}$  and  $4\times10^{-3}\,\mathrm{mbar}$ , with and without  $O_2$ . In Figure 4.18, we can see the performance of the top 5 PSCs produced with each of these layers.

Interestingly, SnO<sub>2</sub> layers sputtered at  $2\times 10^{-3}$  mbar yielded appreciably high  $V_{oc}$  (as high as  $1.05\,V$ ), but far lower  $J_{sc}$  (maximum of  $7.83\,\text{mA/cm}^2$ ). In the case of the  $2\times 10^{-3}$  mbar,  $2.43\,\%$  O<sub>2</sub> cells, the low current may be attributed to the lower transmittance ( $T_{500}=73.45$ ) and far higher resistivity ( $\rho=135.50\,\Omega\,\text{cm}$ ) in comparison to the  $4\times 10^{-3}$  mbar,  $2.43\,\%$  O<sub>2</sub> sample ( $T_{500}=84.65$ ,  $\rho=0.10\,\Omega\,\text{cm}$ ), as both parasitic light absorption and parasitic series resistance would decrease  $J_{sc}$ , without significantly reducing  $V_{oc}$ .

#### 4.2.2 PSCs with RT-SnO<sub>2</sub>

Following the observation that  $SnO_2$  samples sputtered at  $50\,W$  and  $3\times10^{-3}\,mbar$  with  $2.43\,\%$   $O_2$  displayed appreciable conductivity in their as-deposited state, much of the subsequent work was devoted to exploring the potential of this room temperature-processed layer, due both to its compatibility with flexible substrates and to the superior performance of low temperature-processed  $SnO_2$  reported in the literature [48]. On account of these aspects, PSCs with RT-SnO<sub>2</sub> layers were manufactured on rigid ITO-coated glass and flexible ITO-coated PET substrates.

Figure 4.19 shows the performance of these devices. The PSCs manufactured on ITO-coated glass yielded the highest PCE achieved in this work — 12.4 %, with  $V_{oc} = 1.00\,V$ ,  $J_{sc} = 19.8\,\text{mA/cm}^2$  and  $FF = 62.4\,\%$ . The best-performing PSC on ITO-coated PET had a PCE of 9.54 % ( $V_{oc} = 0.89\,V$ ,  $J_{sc} = 21.61\,\text{mA/cm}^2$ ,  $FF = 49.3\,\%$ ), predictably lower than the efficiency of the glass-ITO cell as the sheet resistance of the PET substrate is roughly twice as high.

Several of the manufactured PSCs exhibited significant light-soaking effect, with the performance improving as the light exposure time increased. Figure 4.20 exemplifies the effect of light-soaking on one of the top PSCs on PET-ITO. After 15 s of pre-measurement light exposure, the  $V_{oc}$ ,  $J_{sc}$  and fill factor of the cell significantly increase, increasing further after 30 s before stabilizing. There a several mechanisms proposed for this kind of effect. Primarily, it is thought to emerge from the neutralization of positive defects in the perovskite film and on the electrode interfaces by photogenerated electrons [73], and from photoinduced ion migration within the perovskite film [74]. Ion migration, specifically, is theorized to boost conductivity in the perovskite layer (which is consistent with the observed decrease in series resistance) and enhance band-bending when the ions accumulate at the interface with the charge transport layer (leading to higher  $V_{oc}$ , as observed).

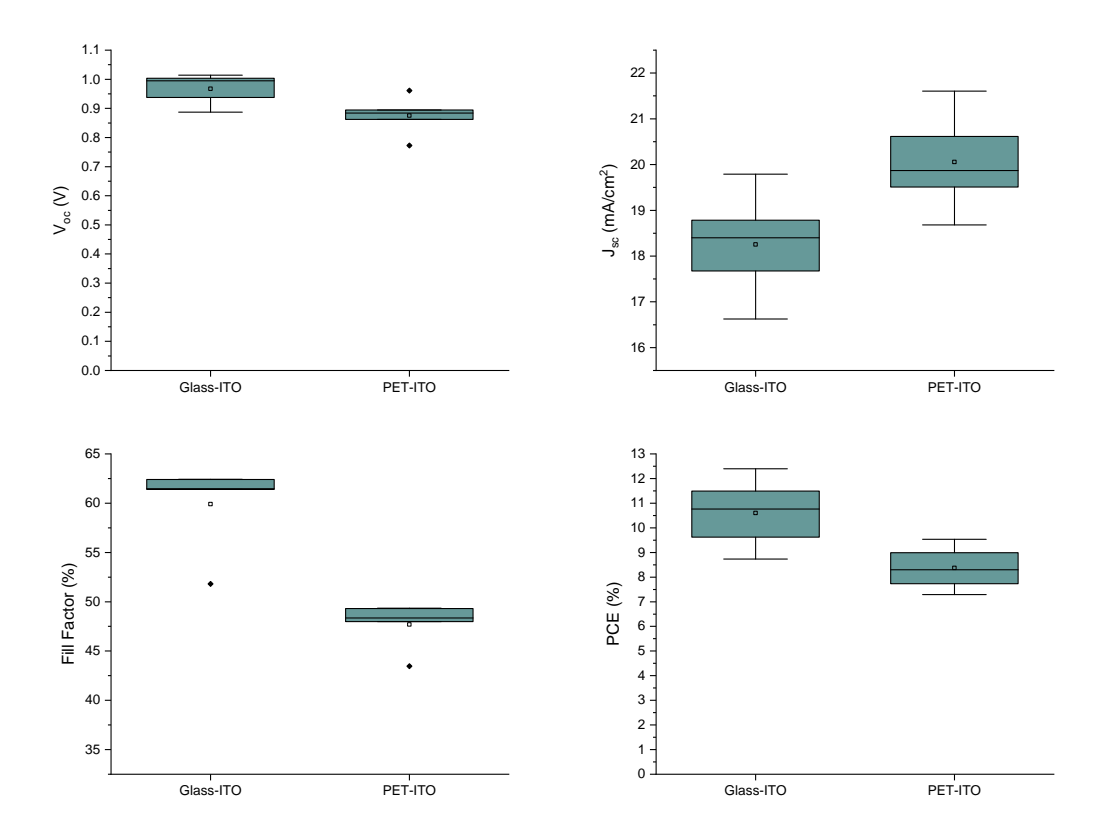


Figure 4.19: Electrical performance of PSCs manufactured with  $SnO_2$  layers sputtered at  $50\,W$ ,  $3\times10^{-3}$  mbar and 2.43 %  $O_2$ , without annealing, on ITO-coated glass and ITO-coated PET. Top 5 solar cells from each batch considered.

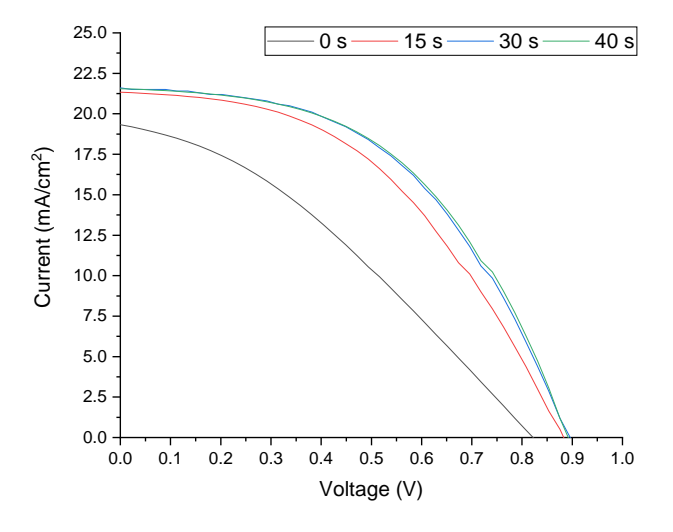


Figure 4.20: Effect of pre-measurement light exposure on the performance of a PSC on PET-ITO, with  $SnO_2$  layers sputtered at  $50\,W$ ,  $3\times10^{-3}$  mbar and  $2.43\,\%$   $O_2$ , without annealing.

### 4.2.3 PSCs with light-trapping structures

Having established the PSCs manufactured in 4.2.2 - PSCs with RT-SnO<sub>2</sub> as a benchmark, the work proceeded with the production of cells on substrates containing ITO light-trapping structures. Among the various structured substrates available, 6 were selected based on their transmittance and sheet resistance (see Appendix B); the characteristics of their production are shown in Table 4.5.

S	ample	PS Sphere Size (µm)	Planar ITO Thickness (nm)	Structured ITO Thickness (nm)	RIE Time (s)
	LT1	0.9	100	150	100
	LT2	0.9	100	150	100
	LT3	1.3	100	150	150
	LT4	1.3	100	200	150
	LT5	1.3	100	150	150
	IT6	1.2	100	200	150

Table 4.5: Characteristics of the selected structured substrates.

To assess the conformality of the  $SnO_2$  layer sputtered on top of the LT structures, cross-sectional SEM-FIB images of the manufactured cells were obtained (Figure 4.21). They show a compact and even layer of  $SnO_2$  that closely follows the geometry of the structured ITO, showing a desired degree of conformality.

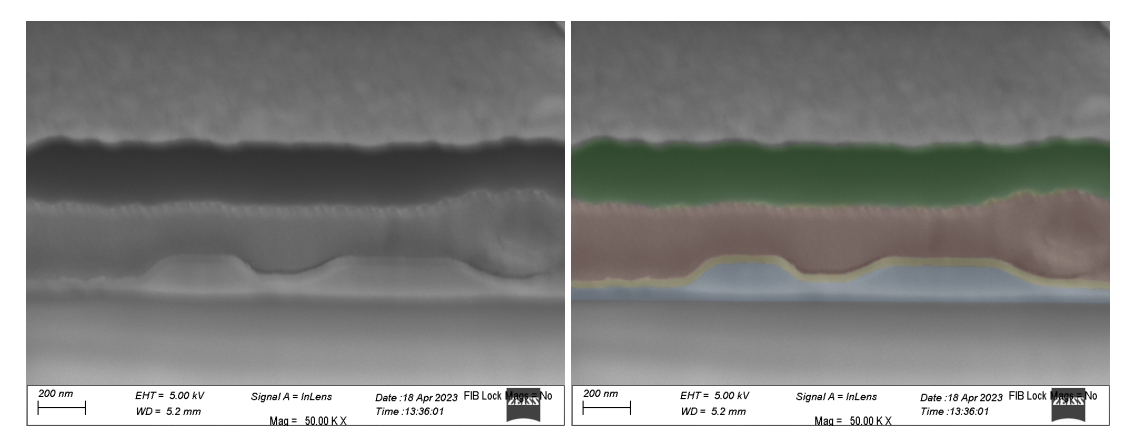


Figure 4.21: Original (left) and colorized (right) SEM-FIB cross-section of perovskite solar cell on LT substrate (0.9 μm PS spheres, with 50 nm ITO planar layer and 150 nm structured ITO layer, 200 s of RIE). Blue: ITO, yellow: SnO<sub>2</sub>, orange: MAPbI<sub>3</sub>, green: spiro-OMeTAD.

The performance of the top PSC manufactured from each substrate is summarized in Table 4.6. Substrates LT1, LT2 and LT5 yielded the best performance, with a top efficiency of 7.41 % achieved for LT2 ( $V_{oc} = 0.85 \, V$ ,  $J_{sc} = 18.07 \, mA/cm^2$ , FF = 48.17 %). While inferior to the benchmark planar cells, these results show that the methods to incorporate light-trapping structures developed in this work can yield working PSCs, with the desired conformal architecture.

It is important to consider that, being themselves experimental, the light-trapping ITO structures utilized suffer from two issues that likely hamper their performance: lower transmittance and significantly higher sheet resistance when compared with commercial ITO substrates. Indeed, it is worth noting that both substrates with greater thickness of structured ITO — LT4 and LT6 (200 nm) — exhibited the lowest performance. It is therefore apparent that the light-trapping ITO structures require further optimization before an adequate comparison between the planar and structured PSCs developed in this work can be made, as the difference in quality between the commercial and sputtered ITO layers likely overshadows any possible photonic gains from incorporating the LT structures.

Table 4.6: Solar performance of PSCs manufactured on the selected structured substrates, with  $SnO_2$  layers sputtered at 50 W,  $3 \times 10^{-3} \text{ mbar}$  and  $2.43 \% O_2$ , without annealing.

Sample	$V_{oc}(V)$	$J_{sc}$ (mA/cm <sup>2</sup> )	Fill Factor (%)	<b>PCE (%)</b>
LT1	0.75	18.01	42.35	5.71
	0.85	17.06	37.74	5.47
	0.80	16.53	40.06	5.32
LT2	0.85	18.07	48.17	7.41
	0.81	17.65	48.44	6.94
	0.68	8.45	45.61	2.63
LT3	0.61	17.92	43.60	4.77
	0.58	15.31	46.43	4.10
	0.61	13.56	49.02	4.05
LT4	0.63	15.61	40.45	3.97
	0.64	12.76	46.37	3.76
	0.55	16.66	39.26	3.57
LT5	0.93	16.65	40.67	6.32
	0.98	15.13	38.75	5.73
	0.89	15.81	40.30	5.70
LT6	0.42	5.73	46.89	1.12
	0.41	4.23	49.55	0.87
	0.38	4.39	49.59	0.83

### 4.2.4 PSC stability

The PSCs developed throughout this work exhibited significant instability, degrading their performance quickly and often rendering them non-functional in only a few days. This instability can likely be attributed to two factors: a) the lack of encapsulation, meaning that the cells are directly exposed to environmental agents (O<sub>2</sub>, moisture, UV) during transfer and measurement of the samples; and b) the lack of passivating layers between the perovskite film and the charge transport layers, as the interfacial contact with SnO<sub>2</sub> [75] and spiro-OMeTAD [27, 76] are known to induce new degradation pathways.

# Conclusions and Future Prospects

In this work, we successfully manufactured good quality, room-temperature processed  $SnO_2$  layers via magnetron RF sputtering at  $50\,\mathrm{W}$  and  $3\times10^{-3}$  mbar with  $2.43\,\%$  oxygen, and demonstrated its conformal deposition on light-trapping ITO substrates manufactured by colloidal lithography, to produce working perovskite solar cells with a structured front electrode.

The highest power conversion efficiencies achieved were 12.4% in planar ITO-coated glass, 9.54% in ITO-coated PET and 7.41% in structured ITO substrate produced from 0.9 µm PS spheres, with 100 nm of planar ITO and 150 nm of structured ITO. While no performance gains could be achieved in this work by the incorporation of light-trapping structures, on account of the need to further optimize the sputtered ITO layer used in its manufacturing before it can be adequately compared to commercial/planar substrates, the feasibility to producing n-i-p superstrate configuration using a conformally sputter-deposited ETL was established, clearing the way for future efficiency gains by photonic structure use.

In the context of this work, we further studied the effect of RF power, working pressure,  $O_2$  content and post-deposition annealing on the properties of the sputtered  $SnO_2$  ETL, developing an understanding of how it can be adequately processed at both high and room temperature for use in perovskite solar cells. Specifically, we found low RF power and higher  $O_2$  contents to promote the formation of thin films with higher transparency, with the addition of  $O_2$  to the sputtering gas mixture effectively suppressing oxygen vacancies, as evidenced by XPS-UPS surveys. Post-deposition annealing was shown to significantly increase the transmittance of  $SnO_2$  films deposited under pure Ar. Annealing displayed a comparatively modest effect on  $SnO_2$  samples deposited under a  $O_2$ /Ar mixture, likely owing to the lower quantity of oxygen vacancies available to react with atmospheric  $O_2$ . Annealing was shown to greatly decrease the resistivity of the  $SnO_2$ , with an accompanying increase in apparent bandgap which may be attributed to Burstein-Moss shift.

In light of the results achieved in this work, we can advise that future work should focus on three key aspects: a) the optimization of the sputtered  $SnO_2$  ETL, which may consist of not only refining the deposition parameters, but also assessing the effect of substrate heating during deposition as well as the possibility of depositing multilayer/gradient ETLs via sputtering; b) the optimization of the structured ITO substrates, improving the quality of the sputtered ITO layers and of the colloidal lithography process to achieve substrates with better conductivity and light-trapping effect; and c) passivation and encapsulation of the PSC layers, as well as interface engineering, in order to improve and stabilize their performance.

### BIBLIOGRAPHY

- [1] Global Market Outlook For Solar Power 2023-2027. SolarPower Europe, 2023-06. URL: https://www.solarpowereurope.org/insights/outlooks/global-market-outlook-for-solar-power-2023-2027/detail(cit.on p. 1).
- [2] 2023 Levelized Cost Of Energy+. Lazard, 2023-04, p. 9. URL: https://www.lazard.com/research-insights/2023-levelized-cost-of-energyplus/(cit. on p. 1).
- [3] J. Liu et al. "Review of status developments of high-efficiency crystalline silicon solar cells". In: *Journal of Physics D: Applied Physics* 51 (12 2018-03), p. 123001. ISSN: 0022-3727. DOI: 10.1088/1361-6463/aaac6d (cit. on p. 1).
- [4] S. He et al. "How far are we from attaining 10-year lifetime for metal halide perovskite solar cells?" In: *Materials Science and Engineering: R: Reports* 140 (2020-04), p. 100545. ISSN: 0927796X. DOI: 10.1016/j.mser.2020.100545 (cit. on p. 1).
- [5] Report on Critical Raw Materials for the EU. EU Ad-Hoc Working Group on Raw Materials, 2014-05. URL: https://ec.europa.eu/docsroom/documents/10010/(cit. on p. 1).
- [6] M. H. Shubbak. "Advances in solar photovoltaics: Technology review and patent trends". In: *Renewable and Sustainable Energy Reviews* 115 (2019-11), p. 109383. ISSN: 13640321. DOI: 10.1016/j.rser.2019.109383 (cit. on p. 1).
- [7] F. Meillaud et al. "Recent advances and remaining challenges in thin-film silicon photovoltaic technology". In: *Materials Today* 18 (7 2015-09), pp. 378–384. ISSN: 13697021. DOI: 10.1016/j.mattod.2015.03.002 (cit. on p. 1).
- [8] B. Commault et al. "Overview and Perspectives for Vehicle-Integrated Photovoltaics". In: *Applied Sciences* 11 (24 2021-12), p. 11598. ISSN: 2076-3417. DOI: 10.3390/app112411598 (cit. on p. 1).
- [9] A. Kojima et al. "Organometal Halide Perovskites as Visible-Light Sensitizers for Photovoltaic Cells". In: *Journal of the American Chemical Society* 131 (17 2009-05), pp. 6050–6051. ISSN: 0002-7863. DOI: 10.1021/ja809598r (cit. on pp. 1, 3).

- [10] Best Research-Cell Efficiency Chart | Photovoltaic Research | NREL. Accessed: 03-08-2023. National Renewable Energy Laboratory. URL: https://www.nrel.gov/pv/cell-efficiency.html (cit. on pp. 1, 3).
- [11] H. S. Jung et al. "Flexible Perovskite Solar Cells". In: *Joule* 3 (8 2019-08), pp. 1850–1880. ISSN: 25424351. DOI: 10.1016/j.joule.2019.07.023 (cit. on p. 2).
- [12] K. A. Bush et al. "Compositional Engineering for Efficient Wide Band Gap Perovskites with Improved Stability to Photoinduced Phase Segregation". In: *ACS Energy Letters* 3 (2 2018-02), pp. 428–435. ISSN: 2380-8195. DOI: 10.1021/acsenergylett. 7b01255 (cit. on pp. 2, 3).
- [13] M. H. Futscher and B. Ehrler. "Efficiency Limit of Perovskite/Si Tandem Solar Cells". In: *ACS Energy Letters* 1 (4 2016-10), pp. 863–868. ISSN: 2380-8195. DOI: 10.1021/acsenergylett.6b00405 (cit. on p. 2).
- [14] S. Rühle. "Tabulated values of the Shockley–Queisser limit for single junction solar cells". In: *Solar Energy* 130 (2016-06), pp. 139–147. ISSN: 0038092X. DOI: 10.1016/j.solener.2016.02.015 (cit. on p. 2).
- [15] Y. Da, Y. Xuan, and Q. Li. "Quantifying energy losses in planar perovskite solar cells". In: *Solar Energy Materials and Solar Cells* 174 (2018-01), pp. 206–213. ISSN: 09270248. DOI: 10.1016/j.solmat.2017.09.002 (cit. on p. 2).
- [16] R. D. Oliveira et al. "Colloidal Lithography for Photovoltaics: An Attractive Route for Light Management". In: *Nanomaterials* 11 (7 2021-06), p. 1665. ISSN: 2079-4991. DOI: 10.3390/nano11071665 (cit. on pp. 2, 6, 17).
- [17] S. Haque et al. "Design of wave-optical structured substrates for ultra-thin perovskite solar cells". In: *Applied Materials Today* 20 (2020-09), p. 100720. ISSN: 23529407. DOI: 10.1016/j.apmt.2020.100720 (cit. on pp. 2, 5, 6).
- [18] M. M. Lee et al. "Efficient hybrid solar cells based on meso-superstructured organometal halide perovskites". In: Science 338 (6107 2012-11), pp. 643-647. ISSN: 10959203. DOI: 10.1126/SCIENCE.1228604. URL: https://www.science.org/doi/10.1126/science.1228604 (cit. on p. 3).
- [19] J. Yan et al. "Progress and challenges on scaling up of perovskite solar cell technology". In: *Sustainable Energy & Fuels* 6 (2 2022), pp. 243–266. ISSN: 2398-4902. DOI: 10.1039/D1SE01045J (cit. on p. 3).
- [20] T.-B. Song et al. "Perovskite solar cells: film formation and properties". In: *Journal of Materials Chemistry A* 3 (17 2015), pp. 9032–9050. ISSN: 2050-7488. DOI: 10.1039 /C4TA05246C (cit. on p. 3).
- [21] Q. A. Akkerman and L. Manna. "What Defines a Halide Perovskite?" In: ACS Energy Letters (2020), pp. 604–610. ISSN: 23808195. DOI: 10.1021/ACSENERGYLETT.0C00039. URL: https://pubs.acs.org/doi/full/10.1021/acsenergylett.0c00039 (cit. on p. 3).

- [22] M. Johnsson and P. Lemmens. "Crystallography and Chemistry of Perovskites". In: Handbook of Magnetism and Advanced Magnetic Materials (2007-12). DOI: 10.1002/9780470022184.HMM411. URL: https://onlinelibrary.wiley.com/doi/full/10.1002/9780470022184.hmm411 (cit. on p. 4).
- [23] S. C. Tidrow. "Mapping Comparison of Goldschmidt's Tolerance Factor with Perovskite Structural Conditions". In: *Ferroelectrics* 470 (1 2014-10), pp. 13–27. ISSN: 0015-0193. DOI: 10.1080/00150193.2014.922372 (cit. on p. 4).
- [24] J. Y. Kim et al. "High-Efficiency Perovskite Solar Cells". In: *Chemical Reviews* 120 (15 2020-08), pp. 7867-7918. ISSN: 0009-2665. DOI: 10.1021/acs.chemrev.0c00107. URL: https://pubs.acs.org/doi/10.1021/acs.chemrev.0c00107 (cit. on p. 4).
- [25] L. Lin et al. "Inorganic Electron Transport Materials in Perovskite Solar Cells". In: Advanced Functional Materials 31 (5 2021-01), p. 2008300. ISSN: 1616-301X. DOI: 10.1002/adfm.202008300. URL: https://onlinelibrary.wiley.com/doi/10.1002/adfm.202008300 (cit. on pp. 4, 7).
- [26] A. Sławek, Z. Starowicz, and M. Lipiński. "The Influence of the Thickness of Compact TiO2 Electron Transport Layer on the Performance of Planar CH3NH3PbI3 Perovskite Solar Cells". In: *Materials* 14 (12 2021-06), p. 3295. ISSN: 1996-1944. DOI: 10.3390/ma14123295 (cit. on p. 4).
- [27] C. C. Boyd et al. "Understanding Degradation Mechanisms and Improving Stability of Perovskite Photovoltaics". In: *Chemical Reviews* 119 (5 2019-03), pp. 3418–3451. ISSN: 0009-2665. DOI: 10.1021/acs.chemrev.8b00336 (cit. on pp. 5, 28).
- [28] S. Ma et al. "Development of encapsulation strategies towards the commercialization of perovskite solar cells". In: *Energy & Environmental Science* 15 (1 2022), pp. 13–55. ISSN: 1754-5692. DOI: 10.1039/D1EE02882K (cit. on p. 5).
- [29] D.-L. Wang et al. "Highly efficient light management for perovskite solar cells". In: *Scientific Reports* 6 (1 2016-01), p. 18922. ISSN: 2045-2322. DOI: 10.1038/srep18922 (cit. on p. 5).
- [30] D. A. Jacobs et al. "Light Management: A Key Concept in High-Efficiency Perovskite/Silicon Tandem Photovoltaics". In: *The Journal of Physical Chemistry Letters* 10 (11 2019-06), pp. 3159–3170. ISSN: 1948-7185. DOI: 10.1021/acs.jpclett.8b03 721 (cit. on p. 5).
- [31] W. Raja et al. "Photon recycling in perovskite solar cells and its impact on device design". In: *Nanophotonics* 10 (8 2021-06), pp. 2023–2042. ISSN: 2192-8614. DOI: 10.1515/nanoph-2021-0067 (cit. on p. 5).
- [32] F. Berry et al. "Light Management in Perovskite Photovoltaic Solar Cells: A Perspective". In: *Advanced Energy Materials* 12 (20 2022-05), p. 2200505. ISSN: 1614-6832. DOI: 10.1002/aenm.202200505 (cit. on p. 5).

- [33] Q. G. Du, G. Shen, and S. John. "Light-trapping in perovskite solar cells". In: *AIP Advances* 6 (6 2016-06). ISSN: 2158-3226. DOI: 10.1063/1.4953336 (cit. on p. 6).
- [34] S. Sun et al. "Light trapping nano structures with over 30% enhancement in perovskite solar cells". In: *Organic Electronics* 75 (2019-12), p. 105385. ISSN: 15661199. DOI: 10.1016/j.orgel.2019.105385 (cit. on p. 6).
- [35] A. Tooghi, D. Fathi, and M. Eskandari. "Numerical study of a highly efficient light trapping nanostructure of perovskite solar cell on a textured silicon substrate". In: *Scientific Reports* 10 (1 2020-10), p. 18699. ISSN: 2045-2322. DOI: 10.1038/s41598-0 20-75630-4 (cit. on p. 6).
- [36] A. Tooghi, D. Fathi, and M. Eskandari. "High-performance perovskite solar cell using photonic–plasmonic nanostructure". In: *Scientific Reports* 10 (1 2020-07), p. 11248. ISSN: 2045-2322. DOI: 10.1038/s41598-020-67741-9 (cit. on p. 6).
- [37] Y. Luo et al. "Perovskite Solar Cells on Corrugated Substrates with Enhanced Efficiency". In: *Small* 12 (46 2016-12), pp. 6346–6352. ISSN: 1613-6810. DOI: 10.1002/smll.201601974 (cit. on p. 6).
- [38] X. Zheng et al. "Designing nanobowl arrays of mesoporous TiO2 as an alternative electron transporting layer for carbon cathode-based perovskite solar cells". In: *Nanoscale* 8 (12 2016), pp. 6393–6402. ISSN: 2040-3364. DOI: 10.1039/C5NR06715D (cit. on p. 6).
- [39] M. T. Hörantner et al. "Templated microstructural growth of perovskite thin films via colloidal monolayer lithography". In: *Energy & Environmental Science* 8 (7 2015), pp. 2041–2047. ISSN: 1754-5692. DOI: 10.1039/C5EE01169H (cit. on p. 6).
- [40] K. Mahmood, S. Sarwar, and M. T. Mehran. "Current status of electron transport layers in perovskite solar cells: materials and properties". In: *RSC Advances* 7 (28 2017), pp. 17044–17062. ISSN: 2046-2069. DOI: 10.1039/C7RA00002B (cit. on p. 7).
- [41] Q. Wali et al. "Tin oxide as an emerging electron transport medium in perovskite solar cells". In: *Solar Energy Materials and Solar Cells* 179 (2018-06), pp. 102–117. ISSN: 0927-0248. DOI: 10.1016/J.SOLMAT.2018.02.007 (cit. on p. 7).
- [42] T. Kim, J. Lim, and S. Song. "Recent Progress and Challenges of Electron Transport Layers in Organic–Inorganic Perovskite Solar Cells". In: *Energies 2020, Vol. 13, Page 5572* 13 (21 2020-10), p. 5572. ISSN: 1996-1073. DOI: 10.3390/EN13215572. URL: https://www.mdpi.com/1996-1073/13/21/5572 (cit. on p. 7).
- [43] G. Yang et al. "Recent progress in electron transport layers for efficient perovskite solar cells". In: *Journal of Materials Chemistry A* 4 (11 2016-03), pp. 3970–3990. ISSN: 2050-7496. DOI: 10.1039/C5TA09011C. URL: https://pubs.rsc.org/en/content/articlehtml/2016/ta/c5ta09011chttps://pubs.rsc.org/en/content/articlelanding/2016/ta/c5ta09011c (cit. on p. 7).

- [44] A. K. Chandiran et al. "Analysis of Electron Transfer Properties of ZnO and TiO2 Photoanodes for Dye-Sensitized Solar Cells". In: *ACS Nano* 8 (3 2014-03), pp. 2261–2268. ISSN: 1936-0851. DOI: 10.1021/nn405535j (cit. on p. 7).
- [45] Z. Li, P. Graziosi, and N. Neophytou. "Electron and Hole Mobility of SnO2 from Full-Band Electron–Phonon and Ionized Impurity Scattering Computations". In: *Crystals* 12 (11 2022-11), p. 1591. ISSN: 2073-4352. DOI: 10.3390/cryst12111591 (cit. on p. 7).
- [46] C. Altinkaya et al. "Tin Oxide Electron-Selective Layers for Efficient, Stable, and Scalable Perovskite Solar Cells". In: *Advanced Materials* 33 (15 2021-04), p. 2005504. ISSN: 0935-9648. DOI: 10.1002/adma.202005504. URL: https://onlinelibrary.wiley.com/doi/10.1002/adma.202005504 (cit. on p. 7).
- [47] D. Leng et al. "Preparation and properties of SnO2 film deposited by magnetron sputtering". In: *International Journal of Photoenergy* 2012 (2012). ISSN: 1687529X. DOI: 10.1155/2012/235971 (cit. on p. 7).
- [48] L. Qiu et al. "Scalable Fabrication of Stable High Efficiency Perovskite Solar Cells and Modules Utilizing Room Temperature Sputtered SnO2 Electron Transport Layer". In: Advanced Functional Materials 29 (47 2019-11), p. 1806779. ISSN: 1616-301X. DOI: 10.1002/adfm.201806779 (cit. on pp. 7, 25).
- [49] Z. Peng et al. "Isolating the Oxygen Adsorption Defects on Sputtered Tin Oxide for Efficient Perovskite Solar Cells". In: *ACS Applied Materials & Interfaces* 15 (19 2023-05), pp. 23518–23526. ISSN: 1944-8244. DOI: 10.1021/acsami.3c03679 (cit. on p. 7).
- [50] H. Lu et al. "Identifying the optimum thickness of electron transport layers for highly efficient perovskite planar solar cells". In: *Journal of Materials Chemistry A* 3 (32 2015), pp. 16445–16452. ISSN: 2050-7488. DOI: 10.1039/C5TA03686K (cit. on p. 10).
- [51] W. Ke et al. "Low-Temperature Solution-Processed Tin Oxide as an Alternative Electron Transporting Layer for Efficient Perovskite Solar Cells". In: *Journal of the American Chemical Society* 137 (21 2015-06), pp. 6730–6733. ISSN: 0002-7863. DOI: 10.1021/jacs.5b01994 (cit. on p. 10).
- [52] R. Jeyakumar et al. "Influence of Electron Transport Layer (TiO2) Thickness and Its Doping Density on the Performance of CH3NH3PbI3-Based Planar Perovskite Solar Cells". In: *Journal of Electronic Materials* 49 (6 2020-06), pp. 3533–3539. ISSN: 0361-5235. DOI: 10.1007/s11664-020-08041-w (cit. on p. 10).
- [53] S. Rossnagel. "Sputtering and Sputter Deposition". In: Handbook of Thin Film Deposition Processes and Techniques: Principles, Methods, Equipment and Applications.
   Ed. by K. Seshan. Second Edition. Noyes Publications, 2002, pp. 319–348. ISBN: 0-8155-1442-5 (cit. on p. 11).

- [54] D Kudryashov, A Gudovskikh, and K Zelentsov. "Low temperature growth of ITO transparent conductive oxide layers in oxygen-free environment by RF magnetron sputtering". In: *Journal of Physics: Conference Series* 461 (2013-08), p. 012021. ISSN: 1742-6596. DOI: 10.1088/1742-6596/461/1/012021 (cit. on p. 11).
- [55] A. Chaoumead, Y. moon Sung, and D.-J. Kwak. "The Effects of RF Sputtering Power and Gas Pressure on Structural and Electrical Properties of ITiO Thin Film". In: *Advances in Condensed Matter Physics* 2012 (2012), pp. 1–7. ISSN: 1687-8108. DOI: 10.1155/2012/651587 (cit. on p. 11).
- [56] M. Chaves et al. "Al-doping and Properties of AZO Thin Films Grown at Room Temperature: Sputtering Pressure Effect". In: *Materials Research* 22 (2 2019). ISSN: 1980-5373. DOI: 10.1590/1980-5373-mr-2018-0665 (cit. on p. 11).
- [57] R Hippler et al. "Ion formation in an argon and argon-oxygen gas mixture of a magnetron sputtering discharge". In: *Journal of Physics Communications* 3 (5 2019-05), p. 055011. ISSN: 2399-6528. DOI: 10.1088/2399-6528/ab1e82 (cit. on p. 12).
- [58] P. D.M. et al. "Effect of annealing ambient on SnO2 thin film transistors". In: *Applied Surface Science* 418 (2017-10), pp. 414–417. ISSN: 01694332. DOI: 10.1016/j.apsusc.2016.11.233 (cit. on p. 13).
- [59] J. Park et al. "The effect of post-annealing on Indium Tin Oxide thin films by magnetron sputtering method". In: *Applied Surface Science* 307 (2014-07), pp. 388–392. ISSN: 01694332. DOI: 10.1016/j.apsusc.2014.04.042 (cit. on p. 14).
- [60] A. Lyubchyk et al. "Influence of post-deposition annealing on electrical and optical properties of ZnO-based TCOs deposited at room temperature". In: *physica status solidi (a)* 213 (9 2016-09), pp. 2317–2328. ISSN: 18626300. DOI: 10.1002/pssa.20153 2891 (cit. on p. 14).
- [61] R. G. Goodchild, J. B. Webb, and D. F. Williams. "Electrical properties of highly conducting and transparent thin films of magnetron sputtered SnO2". In: *Journal of Applied Physics* 57 (6 1985-03), pp. 2308–2310. ISSN: 0021-8979. DOI: 10.1063/1.334 331 (cit. on p. 16).
- [62] A. Karoui. "Aluminum Ultra Thin Film Grown by Physical Vapor Deposition for Solar Cell Electric Nanocontacts". In: *ECS Transactions* 41 (4 2011-10), pp. 21–28. ISSN: 1938-5862. DOI: 10.1149/1.3628605 (cit. on p. 16).
- [63] J. Siegel et al. "Annealing of gold nanostructures sputtered on polytetrafluoroethylene". In: *Nanoscale Research Letters* 6 (1 2011-11), p. 588. ISSN: 1556-276X. DOI: 10.1186/1556-276X-6-588 (cit. on p. 16).
- [64] S. W. Kang et al. "Effects of Sn Concentration on Ultrathin ITO Films Deposited Using DC Magnetron Sputtering". In: *Journal of Nanoelectronics and Optoelectronics* 7 (5 2012-10), pp. 494–497. ISSN: 1555-130X. DOI: 10.1166/jno.2012.1375 (cit. on p. 16).

- [65] L. O. L. Cunff, H. Kadiri, and G. Lérondel. "Microscopic defects as the limiting factor in the direct transmission of nanocoatings obtained through self-assembly". In: *Nano Select* 2 (1 2021-01), pp. 140–145. ISSN: 2688-4011. DOI: 10.1002/nano.202000095 (cit. on p. 17).
- [66] D. Fang et al. "Calibration of Binding Energy Positions with C1s for XPS Results". In: *Journal of Wuhan University of Technology-Mater. Sci. Ed.* 35 (4 2020-08), pp. 711–718. ISSN: 1000-2413. DOI: 10.1007/s11595-020-2312-7 (cit. on p. 18).
- [67] V. I. Alekseev, Y. B. Marin, and O. L. Galankina. "An Extreme Concentration of Isomorphic Tantalum in Cassiterite from Lithium–Fluoric Granites (Arga-Ynnakh-Khaysky Massif, Yakutia)". In: *Doklady Earth Sciences* 490 (2 2020-02), pp. 65–67. ISSN: 1028-334X. DOI: 10.1134/S1028334X2002004X (cit. on p. 19).
- [68] M. Kwoka et al. "XPS study of the surface chemistry of L-CVD SnO2 thin films after oxidation". In: *Thin Solid Films* 490 (1 2005-10), pp. 36–42. ISSN: 00406090. DOI: 10.1016/j.tsf.2005.04.014 (cit. on pp. 19, 20).
- [69] M. Batzill. "Surface Science Studies of Gas Sensing Materials: SnO2". In: Sensors 6 (10 2006-10), pp. 1345–1366. ISSN: 1424-8220. DOI: 10.3390/s6101345 (cit. on p. 20).
- [70] S. Saipriya, M. Sultan, and R. Singh. "Effect of environment and heat treatment on the optical properties of RF-sputtered SnO2 thin films". In: *Physica B: Condensed Matter* 406 (4 2011-02), pp. 812–817. ISSN: 09214526. DOI: 10.1016/j.physb.2010.12.003 (cit. on p. 21).
- [71] M. Dkhili et al. "Attributes of High-Performance Electron Transport Layers for Perovskite Solar Cells on Flexible PET versus on Glass". In: ACS Applied Energy Materials 5 (4 2022-04), pp. 4096–4107. ISSN: 2574-0962. DOI: 10.1021/acsaem.1c03 311 (cit. on p. 21).
- [72] B. Čolović et al. "Wetting properties of titanium oxides, oxynitrides and nitrides obtained by DC and pulsed magnetron sputtering and cathodic arc evaporation". In: *Materials Science-Poland* 37 (2 2019-06), pp. 173–181. ISSN: 2083-134X. DOI: 10.2478/msp-2019-0031 (cit. on p. 22).
- [73] C. Zhao et al. "Revealing Underlying Processes Involved in Light Soaking Effects and Hysteresis Phenomena in Perovskite Solar Cells". In: *Advanced Energy Materials* 5 (14 2015-07), p. 1500279. ISSN: 16146832. DOI: 10.1002/aenm.201500279 (cit. on p. 25).
- [74] T. Zhang et al. "Pinning Down the Anomalous Light Soaking Effect toward High-Performance and Fast-Response Perovskite Solar Cells: The Ion-Migration-Induced Charge Accumulation". In: *The Journal of Physical Chemistry Letters* 8 (20 2017-10), pp. 5069–5076. ISSN: 1948-7185. DOI: 10.1021/acs.jpclett.7b02160 (cit. on p. 25).

- [75] J. Gong et al. "Progress in Surface Modification of SnO <sub>2</sub> Electron Transport Layers for Stable Perovskite Solar Cells". In: *Small Science* 3 (6 2023-06). ISSN: 2688-4046. DOI: 10.1002/smsc.202200108 (cit. on p. 28).
- [76] F. M. Rombach, S. A. Haque, and T. J. Macdonald. "Lessons learned from spiro-OMeTAD and PTAA in perovskite solar cells". In: *Energy & Environmental Science* 14 (10 2021), pp. 5161–5190. ISSN: 1754-5692. DOI: 10.1039/D1EE02095A (cit. on p. 28).

# Substrate and solution preparation

### A.1 Light-trapping structure manufacturing

### A.1.1 Substrate preparation

ITO-coated glass measuring  $2.5\,\mathrm{cm} \times 2.5\,\mathrm{cm}$ , manufactured by RF magnetron sputtering, were used as a substrate for the photonic microstructures. The substrates were washed with a MICRO-90 concentrated alkaline cleaning solution and rinsed with deionised water. They were then sonicated for 10 minutes in acetone and isopropanol for the same period and rinsed again with deionised water. Finally, the substrates were dried under a stream of nitrogen.

### A.1.2 Deposition of the PS colloidal monolayer

Polystyrene (PS) colloidal spheres dispersed in aqueous solution at a 2.5 % weight were purchased from Microparticles GmbH, with diameters of 0.9 and 1.3 µm. They were first dispersed in a 1:3 mixture of the aqueous solution and diacetone, and this colloidal suspension was used to deposit a hexagonal close-packed monolayer of PS microspheres via Langmuir-Blodgett (LB) wet coating employing a Biolin Scientific KSV NIMA trough. The deposition consists in dropping 800 mL of the prepared colloidal suspension on the interface between water and air. The barriers of the LB system are then closed at a controlled speed of 10 mm min<sup>-1</sup>, leading the floating PS spheres to self-assemble in an ordered closed-packed hexagonal array at the water surface. Subsequently, this mono-layer is transferred to the surface of the ITO-coated glass substrates by vertically withdrawing the previously immersed substrate at a speed of 2 mm min<sup>-1</sup>.

### A.1.3 Shaping of the colloidal mask

The size and shape of the PS spheres will determine the geometry of the resulting surface structure. Since the colloids are deposited by LB in a closed-packed array, it is necessary to increase the inter-sphere spacing in a controllable manner, in order to create non-closed packed monolayers. This is achieved by partially etching the particles via reactive ion etching (RIE), which decreases the particles' size, hence increasing their spacing. This RIE process is performed with O<sub>2</sub> gas, in an Alcatel GIR300 dry-etching system, using the conditions in the first line of Table A.1.

Table A.1: Experimental conditions used during the two reactive ion etching (RIE) processes carried out in the colloidal lithography fabrication process used for this work.

RIE Atmosphere	Etched Material	Time, t <sub>RIE</sub> (s)	RIE Power (W)	Gas Pressure (mTorr)	Plasma flow (sccm)
-O <sub>2</sub>	Polystyrene	150	50	50	50
Ar/CF <sub>4</sub>	ITO	180	100	100	4/16

### A.1.4 ITO deposition

Indium tin oxide (ITO) films with thickness of 100 and 200 nm, were deposited by radio frequency (RF) magnetron sputtering using an ITO target (99.99 % purity, 3 inches in diameter) in a mixture of oxygen and argon at partial pressures of  $1 \times 10^{-5}$  and  $1.6 \times 10^{-3}$  mbar, for 40 and 150 min, respectively. The applied RF power was 35 W, yielding a deposition rate of 2.5 nm min<sup>-1</sup>. A pre-sputtering process of 15 minutes was performed before deposition to clean the target.

#### A.1.5 Colloidal mask lift-off

The last step of the CL fabrication process consisted in removing the PS particles by sonication of the samples in a toluene bath for 30 minutes. Before that, an  $Ar/CF_4$  RIE process (see Table A.1), was performed to remove the top covering layer of the deposited ITO over the PS particles, promoting the subsequent dissolution of the PS particles in the toluene bath.

# A.2 Substrate cleaning

Soda lime glass and ITO-coated glass substrates were cut into  $2.5 \, \text{cm} \times 2.5 \, \text{cm}$  squares, and cleaned in an ultrasonic bath, using a cleaning solution of 1 vol-% Hellmanex<sup>TM</sup> III in DI water for 40 minutes at 40 °C. Substrates were rinsed 3 times with DI water, followed by 20 minutes of room-temperature ultrasonic cleaning in plain DI water, 15 minutes in acetone and 15 minutes in IPA.

For cleaning ITO-coated PET substrates, the acetone washing step was skipped, to prevent damage to the substrate. After cleaning, the substrates were dried with a nitrogen blow gun and stored vertically in a Wash-N-Dry<sup>TM</sup> rack.

LT structure substrates were cleaned in a room-temperature ultrasonic bath for 20 minutes in acetone and 20 minutes in IPA, followed by drying with a nitrogen blow gun. Finally, LT structures were subjected to an oxygen plasma treatment for 3 minutes, at 70 W and O<sub>2</sub> pressure of 0.4 mbar, for deep removal of organic contaminants.

For substrates destined to solar cell manufacturing, one edge of the substrates was covered with Kapton® tape to create a bare ITO contact with an area of approximately 25 mm by 5 mm once removed.

### A.3 Solution preparation

All solutions were prepared, stored, and used in a glovebox with a protective N<sub>2</sub> atmosphere. MAPbI<sub>3</sub> and spiro-OMeTAD solutions were prepared the day immediately before use.

MAPbI $_3$  solutions were prepared by weighting equal molar amounts of the precursors MAI and PbI $_2$  and dissolving in a ratio of 9:1 DMF to DMSO by volume, to obtain the desired concentration of either 1 M or 1.2 M. The solution was stirred at 60 °C for 4 hours, before being left to stir overnight at room temperature. Immediately before use, MAPbI $_3$  was filtered through a 0.22  $\mu$ m PTFE syringe filter to remove undissolved and foreign matter.

Spiro-OMeTAD solutions were prepared by weighting 75 mg of the reagent per mL of solution and dissolving in the corresponding volume of chlorobenzene. Immediately before use,  $28.8 \,\mu\text{L}$  of 4-tert butylpyridine and  $17.5 \,\mu\text{L}$  of  $0.520 \,g/\text{mL}$  LiTFSI solution in acetonitrile were added as additives per mL of spiro-OMeTAD solution.

# Supplementary information

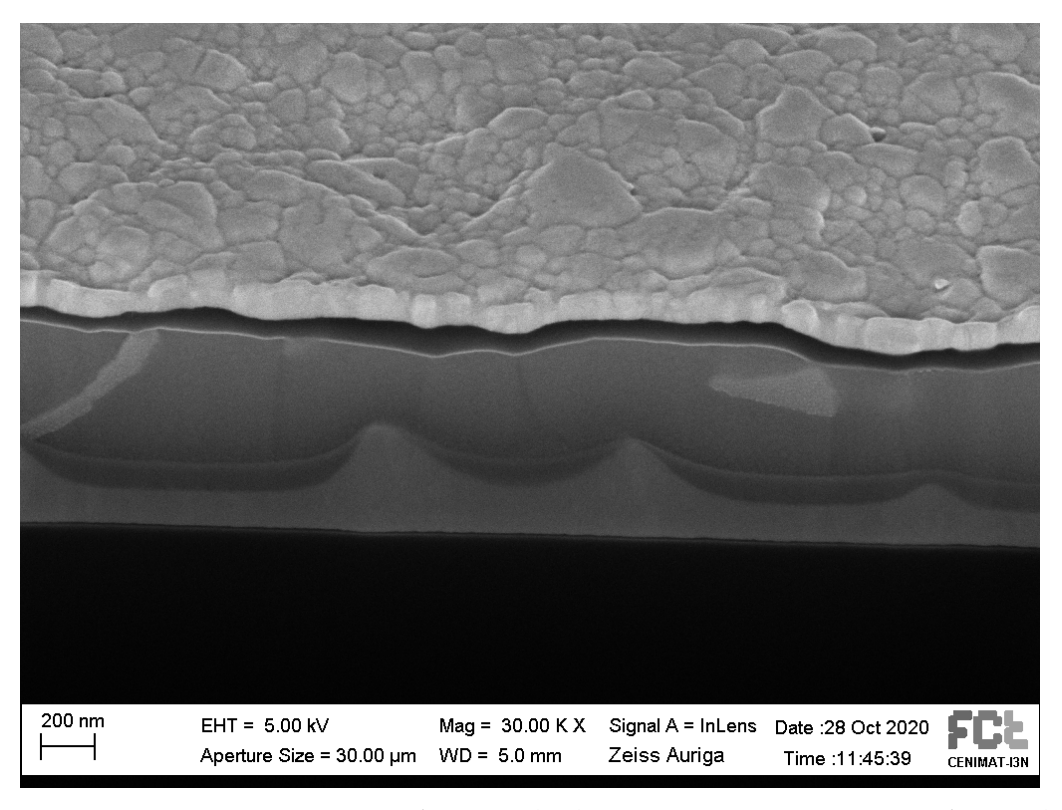


Figure B.1: SEM-FIB cross-section of PSC with photonic IZO structures manufactured via colloidal lithography (1.3  $\mu$ m spheres, 350 nm sputtered IZO, 90 s RIE) and spin-coated SnO<sub>2</sub>, produced in the context of the APOLO project.

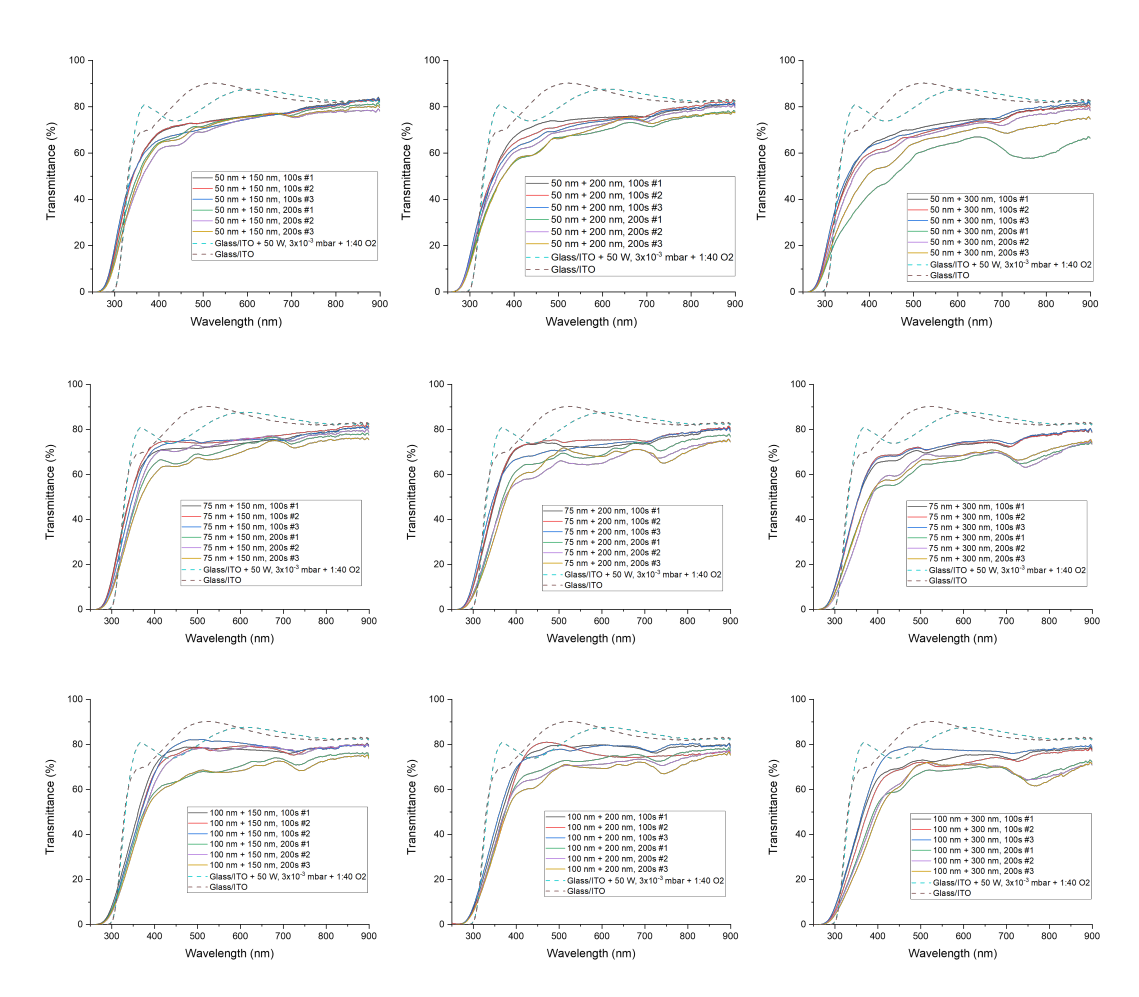


Figure B.2: UV-Vis transmittance of the LT substrates manufactured with 0.9  $\mu m$  PS spheres that were considered for use in the present work.

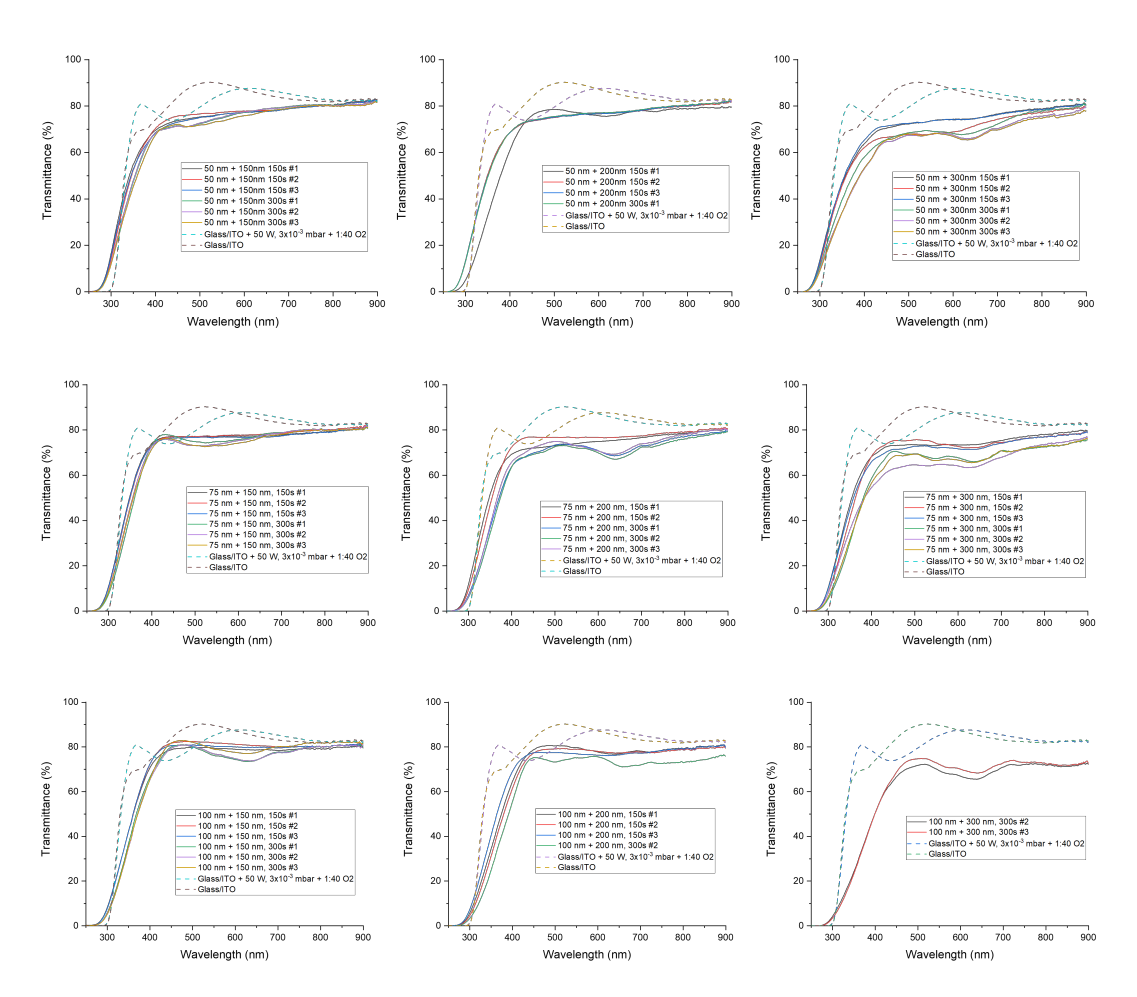


Figure B.3: UV-Vis transmittance of the LT substrates manufactured with 1.3  $\mu m$  PS spheres that were considered for use in the present work.

Table B.1: Sheet resistance of the LT substrates that were considered for use in the present work.

Sample	$\mathbf{Rs_1}$ ( $\Omega/\Box$ )	Rs <sub>2</sub> ( $\Omega/\Box$ )	Rs <sub>3</sub> ( $\Omega/\Box$ )
0.9 μm, 50 nm, 150 nm, 100 s	87	89	148
$0.9  \mu m$ , $50  nm$ , $150  nm$ , $200  s$	70	77	66
$0.9  \mu m$ , $50  nm$ , $200  nm$ , $100  s$	92	87	84
$0.9  \mu m$ , $50  nm$ , $200  nm$ , $200  s$	65	75	78
$0.9  \mu m$ , $50  nm$ , $300  nm$ , $100  s$	80	109	114
$0.9\mu m$ , $50n m$ , $300n m$ , $200s$	72	69	60
0.9 μm, 75 nm, 150 nm, 100 s	110	78	59
$0.9  \mu m$ , $75  nm$ , $150  nm$ , $200  s$	52	50	52
0.9 μm, 75 nm, 200 nm, 100 s	58	59	85
0.9 μm, 75 nm, 200 nm, 200 s	47	45	45
$0.9  \mu m$ , $75  nm$ , $300  nm$ , $100  s$	65	55	62
$0.9\mu m$ , $75n m$ , $300n m$ , $200s$	52	43	47
0.9 μm, 100 nm, 150 nm, 100 s	50	42	41
0.9 μm, 100 nm, 150 nm, 200 s	62	39	54
0.9 μm, 100 nm, 200 nm, 100 s	41	1009	51
0.9 μm, 100 nm, 200 nm, 200 s	46	48	51
0.9 μm, 100 nm, 300 nm, 100 s	61	43	47
0.9 µm, 100 nm, 300 nm, 200 s	40	36	35
1.3 μm, 50 nm, 150 nm, 150 s	89	72	68
$1.3  \mu m$ , $50  nm$ , $150  nm$ , $300  s$	56	55	56
$1.3  \mu m$ , $50  nm$ , $200  nm$ , $150  s$	37	71	66
1.3 μm, 50 nm, 200 nm, 300 s	66		
$1.5  \mu m$ , $50  nm$ , $300  nm$ , $150  s$	64	64	66
1.5 μm, 50 nm, 300 nm, 300 s	54	47	53
1.3 μm, 75 nm, 150 nm, 150 s	54	54	57
1.3 µm, 75 nm, 150 nm, 300 s	47	48	48
1.3 μm, 75 nm, 200 nm, 150 s	72	51	
1.3 μm, 75 nm, 200 nm, 300 s	44	36	38
1.5 μm, 75 nm, 300 nm, 150 s	57	53	63
1.5 μm, 75 nm, 300 nm, 300 s	38	50	37
1.3 μm, 100 nm, 150 nm, 150 s	46	41	47
1.3 μm, 100 nm, 150 nm, 300 s	39	38	37
1.3 μm, 100 nm, 200 nm, 150 s	38	38	44
1.3 μm, 100 nm, 200 nm, 300 s	33	28	28
1.3 μm, 100 nm, 300 nm, 150 s	39	38	38
1.3 µm, 100 nm, 300 nm, 300 s	33	34	35



\_ 2023